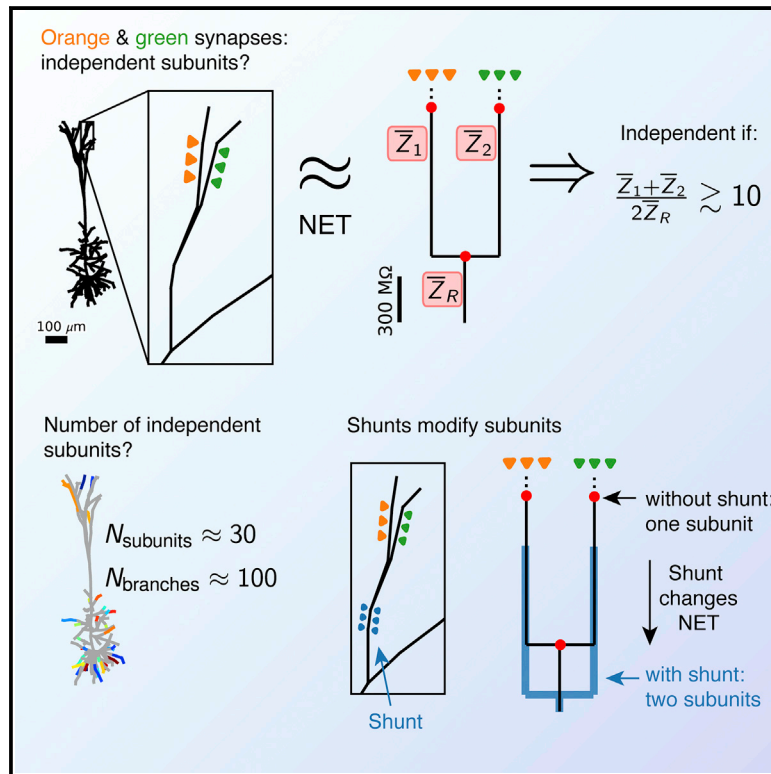


Electrical Compartmentalization in Neurons

Graphical Abstract



Authors

Willem A.M. Wybo,
Benjamin Torben-Nielsen,
Thomas Nevian, Marc-Oliver Gewaltig

Correspondence

btorbennielsen@gmail.com

In Brief

Many neuronal computations rely on the compartmentalization of dendrites into functional subunits. Wybo et al. investigate the number of these subunits that can coexist on a neuron. They find that there are substantially fewer subunits than dendritic branches but that subunit extent and number can be modified by synaptic inputs.

Highlights

- Neural computation relies on compartmentalized dendrites to discern inputs
- A method is described to systematically derive the degree of compartmentalization
- There are substantially fewer functional compartments than dendritic branches
- Compartmentalization is dynamic and can be tuned by synaptic inputs



Electrical Compartmentalization in Neurons

Willem A.M. Wybo,^{1,2,3} Benjamin Torben-Nielsen,^{4,5,6,*} Thomas Nevian,³ and Marc-Oliver Gewaltig¹

¹Blue Brain Project, École Polytechnique Fédérale de Lausanne, Geneva, Switzerland

²Laboratory of Computational Neuroscience, École Polytechnique Fédérale de Lausanne, Lausanne, Switzerland

³Department of Physiology, University of Bern, Bern, Switzerland

⁴Biocomputation Group, University of Hertfordshire, Hertfordshire, UK

⁵NeuroInx Research Institute, La Jolla, CA, USA

⁶Lead Contact

*Correspondence: btorbennielsen@gmail.com

<https://doi.org/10.1016/j.celrep.2019.01.074>

SUMMARY

The dendritic tree of neurons plays an important role in information processing in the brain. While it is thought that dendrites require independent subunits to perform most of their computations, it is still not understood how they compartmentalize into functional subunits. Here, we show how these subunits can be deduced from the properties of dendrites. We devised a formalism that links the dendritic arborization to an impedance-based tree graph and show how the topology of this graph reveals independent subunits. This analysis reveals that cooperativity between synapses decreases slowly with increasing electrical separation and thus that few independent subunits coexist. We nevertheless find that balanced inputs or shunting inhibition can modify this topology and increase the number and size of the subunits in a context-dependent manner. We also find that this dynamic re-compartmentalization can enable branch-specific learning of stimulus features. Analysis of dendritic patch-clamp recording experiments confirmed our theoretical predictions.

INTRODUCTION

Brain function emerges from the orchestrated behavior of billions of individual neurons that transform electrical inputs into action potential (AP) output. This transformation starts on the dendritic tree, where inputs are collected, and proceeds to the axon initial segment where APs are generated before they are transmitted to downstream neurons through the axon. While axons appear to merely communicate the neuronal output downstream, dendrites collect and nonlinearly transform the input. This phenomenon, termed dendritic computation, has been shown to occur *in vivo* and to be required for normal brain function (Grienberger et al., 2015). In both experimental and theoretical work, an abundance of dendritic computations have been proposed (London and Häusser, 2005; Silver, 2010; Torben-Nielsen and Stiefel, 2010). Nearly all of them assume that dendrites are compartmentalized into independent subunits: regions on the dendritic tree that can integrate inputs independently from other regions.

The computational significance of these subunits arises from their ability to support independent regenerative events, such as N-methyl D-aspartate (NMDA), Ca²⁺, or Na⁺ spikes (Wei et al., 2001). These events, where an initial depolarization is enhanced supralinearly by subsequent synaptic inputs and/or voltage-dependent ion-channel currents (Major et al., 2013), significantly strengthen the computational power of neurons. They enable the local decoding of bursts of inputs (Polsky et al., 2009) and hence, through branch-specific plasticity (Goldring et al., 2002; Govindarajan et al., 2011; Losonczy et al., 2008; Weber et al., 2016), drive the clustering of correlated synaptic inputs (Gökçe et al., 2016; Larkum and Nevian, 2008; Lee et al., 2016). A recent finding that distal apical dendrites can spike 10-fold more often than somata (Moore et al., 2017) suggests an important role for this branch-specific plasticity. Independent subunits furthermore allow different input streams to be discriminated from each other (Johanning et al., 2009), and they facilitate sensory perception through feedback signals (Takahashi et al., 2016).

When triggered independently, these local regenerative events are predicted to enable individual neurons to function as two-layer neural networks (Poirazi et al., 2003a, 2003b). This in turn should enable neurons to learn linearly nonseparable functions (Schuessler et al., 2016) and implement translation invariance (Mel et al., 1998). On the network level, independent subunits are thought to dramatically increase memory capacity (Poirazi and Mel, 2001), to allow for the stable storage of feature associations (Bono and Clopath, 2017), represent a powerful mechanism for coincidence detection (Chua and Morrison, 2016; Larkum et al., 1999), and support the back-prop algorithm to train neural networks (Guerguiev et al., 2017; Sacramento et al., 2017; Urbanczik and Senn, 2014).

Thus, abundant data show that dendritic trees consist of a multitude of subunits, and both experimental and theoretical work suggests an important computational role for these subunits (Major et al., 2013). Nevertheless, to date, there is no criterion to quantify the conditions under which regions on the dendrite support the independent triggering of regenerative events, and there is no clear idea about the number of such subunits that can coexist on a given dendritic tree. The most prevalent hypothesis likens dendritic subunits to individual branches (Branco and Häusser, 2010).

In this work, we develop a computational method to answer these questions. We link the dendritic arborization to an



impedance-based tree graph and show how the topology of this tree graph reveals independent subunits. We find that even though voltage may decay sharply toward branchpoints, the remaining depolarization can still cause cooperative dynamics, hence limiting the number of compartments that coexist on dendritic trees. We show that the degree of cooperativity between synapses can be summarized with a single, measurable number, which we term the impedance-based independence index (I_Z). We compute this index from dendritic patch-clamp recordings from basal dendrites of layer 5 (L5) pyramidal neurons in the somatosensory cortex (Nevian et al., 2007) and find the obtained values to agree with our models. We finally demonstrate that compartmentalization is not a static concept but can be regulated dynamically, since balanced inputs or shunting inhibition can modify the topology of the impedance-based tree graph and increase compartmentalization in a global or a highly local manner. This increase in compartmentalization can decorrelate synaptic weight dynamics and hence enable the branch-specific learning of stimulus features.

RESULTS

A Drastic Simplification of the “Connectivity Matrix” of a Neuron

Formalizing the concept of a dendritic subunit requires studying the generation of local regenerative events in conjunction with the electrical separation between synapses. Consider the following scenario: if we were to depolarize a dendritic branch by an amount ΔV (for instance, by injecting a current), then we would alter the probability for local synapses to elicit regenerative events (for instance, through the voltage dependence of synaptic currents such as the NMDA current; Jahr and Stevens, 1990a; MacDonald and Wojtowicz, 1982). If ΔV were small enough, then the change in this probability would be negligible, and the local synapses could be considered independent with respect to the perturbation. In the brain, these changes in voltage are caused by synapses elsewhere in the dendritic tree, which may also elicit regenerative events themselves. Thus, we must ask whether regenerative events elicited elsewhere are attenuated to a sufficient level, allowing local synapses to elicit regenerative events independently.

However, under conditions in which many synapses are active, it is difficult to untangle the loci of origin of the fluctuations at any one dendritic site. Fluctuations that facilitated local regenerative events may have originated in nearby sibling branches, more centripetal or centrifugal branches, or wholly different subtrees. Additionally, the degree to which these fluctuations propagate to any other locus on the neuron is not fixed but depends on all other inputs through synaptic shunting (Gidon and Segev, 2012). Thus, fluctuations at any one site are a tangled, context-dependent combination of the inputs at all other sites. Here, we solve this “tangling” problem by expressing the voltage in a way that these fluctuations are never tangled in the first place: we express the dendritic voltage as a superposition of voltage components at different spatial scales (Figure 1A).

Our model of superimposed voltage components can be visualized as a tree graph, which we term the neural evaluation tree (NET), where each node represents such a component and inte-

grates only inputs arriving into its subtree (Figure 1A, right). The root node of the tree (yellow node in Figure 1A) integrates all inputs to the neuron, whereas the leaf nodes (pink and blue nodes in Figure 1A) only integrate inputs in parts of local subtrees or branches. In this tree, the locus of origin of fluctuations is readily available: if fluctuations that influence regenerative events at synapses 1 and 2 originated at synapse 3, then they would be visible in the voltage component of the green node in Figure 1A. Thus, if the green node contributed to regenerative events at synapses 1 and 2, then these synapses could not be independent from synapse 3. Conversely, if voltage fluctuations in the yellow node do not contribute to regenerative events at synapses 1 and 2, then these synapses must be independent from synapses 4 and 5.

Both the shape and the electrical properties of the dendritic tree determine the interplay between the voltage components; we must accurately estimate the voltage change following any one synaptic input throughout the whole dendritic tree. This suggests starting from the impedance matrix associated with a dendrite. This matrix (already hypothesized to be related to the dendritic compartmentalization; Cuntz et al., 2010) can be seen as the connectivity matrix of a neuron: Each element $Z_{x',x}$ describes how an input current at location x along the dendrite will change the voltage at any location x' . In prior work, the values $Z_{x',x}$ of this matrix (termed input impedances when $x=x'$ and transfer impedances when $x \neq x'$) were used to shed light on the processing properties of various cell types (Koch et al., 1982, 1983) and interactions between synaptic conductances (Gidon and Segev, 2012; Koch et al., 1990).

As we aim to approximate both the spatial and temporal neural dynamics, the impedance matrix is in fact a matrix of temporal kernels $Z_{x',x}(t)$. Each node must furthermore capture an average interaction between synapses; in Figure 1A, the pink node captures interactions between synapses 1 and 2, the green node between 1 and 3 and between 2 and 3, the blue node between 4 and 5, and the yellow node between 1 and 4, 1 and 5, 2 and 4, 2 and 5, 3 and 4, and 3 and 5. Thus, we construct an impedance kernel associated with a node as the average of the transfer impedance kernels between synapses for which that particular node captures the interactions. As we will see, the NET is constructed so that all interactions captured by a single node are approximately equal in amplitude. Furthermore, impedance kernels with equal steady-state impedance values share similar timescales (Figure 1B) so that averaging indeed yields accurate dynamics. While some variation is visible in these kernels on timescales smaller than 0.5 ms, the effect of these variations on the voltage dynamics is negligible, since input currents in general vary more slowly.

We illustrate our NET derivation algorithm on a granule cell (Figures 1C–1I). The dendritic impedance matrix, which is ordered by unraveling the morphology in a depth-first manner (Russell and Norvig, 2003; Figures S1A–S1C), supports a tree-like description; a relatively even blue surface covers most of the matrix (Figure 1D), representing transfer impedances between main dendritic branches. Note that to a good approximation, these impedances indeed have similar magnitudes. Closer to the diagonal, squares of light blue are present, representing dendritic subtrees whose branches are electrically closer to

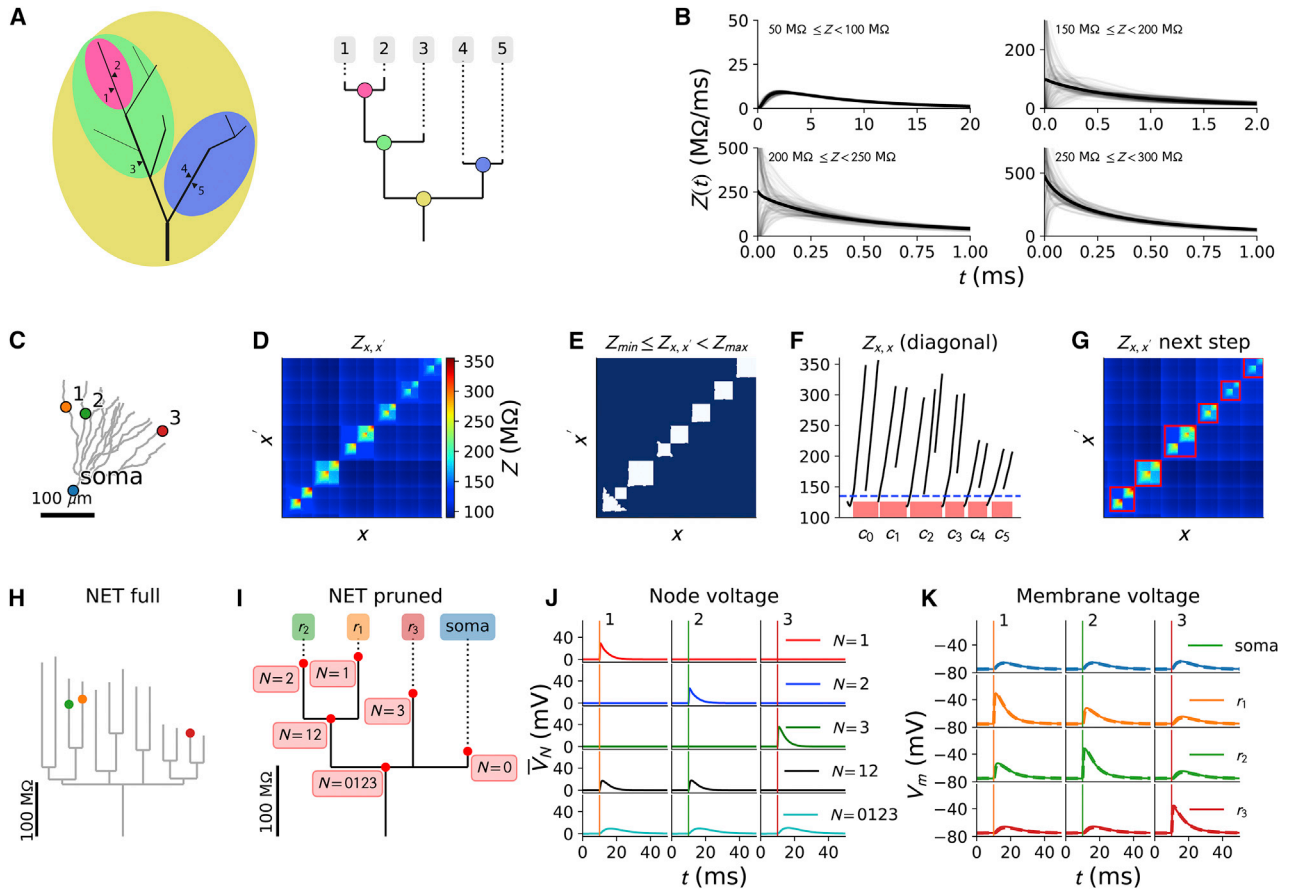


Figure 1. Construction of the NET

(A) Schematic depiction of the NET. The dendrite voltage is obtained as a superposition of voltage components (left) at different spatial scales. The structure of this superposition can be represented graphically as a tree graph (right).

(B) Average impedance kernels for impedances within the indicated ranges on a granule cell.

(C) Granule cell dendrite with three inputs regions (numbers 1–3) and somatic readout.

(D) Impedance matrix associated with the granule cell (morphology is unraveled in a depth-first manner [Russell and Norvig, 2003]; see also Figures S1A–S1C). Color encodes the impedance between each pair of points.

(E) Points in the impedance matrix of the granule cell where the impedance is between $Z_{\min,0}$ (i.e., the minimal transfer impedance in the cell) and $Z_{\max,0}$ ($= 135 \text{ M}\Omega$, chosen for illustrative purposes) are colored blue. The average of the impedance kernels associated with these points will constitute the impedance kernel of the NET root.

(F) Input impedance (diagonal of the impedance matrix). Connected domains with input impedance larger than $Z_{\max,0}$ are indicated on the x axis and denoted by c_i ; they will constitute the child nodes of the NET root.

(G) Impedance matrix with dendritic domains associated with each child node c_i marked by a red square. These restricted matrices are used in the next step of the recursive algorithm.

(H) Full NET for the granule cell. Nodes where inputs from regions 1 to 3 arrive are indicated in the corresponding color.

(I) Pruned NET obtained by removing all nodes that do not integrate regions 1–3.

(J) NET voltages components after an input to location 1 (left), 2 (middle), and 3 (right) (onset indicated with a vertical line, its color matching the input location in (C)). Leaf voltage components ($N=0, 1, 2, 3$) are unique to the associated regions while other nodal voltage components ($N=12$ and $N=0123$) are shared between regions.

(K) Dendritic voltages for the soma and input regions (r_1 – r_3), obtained by summing the nodal voltage components on the path from root to associated leaf. NET traces (dashed lines) agrees with the equivalent NEURON model (full lines).

each other than to other dendritic subtrees. On the diagonal, one finds small squares of green and red colors representing individual terminal branches. First, the impedance kernel of the global node (root node of the tree) is defined by averaging impedance kernels that relate inputs on different main branches (Figure 1E). Then, regions of the dendrite that are electrically closer to each

other than to other regions are identified as connected regions where the input impedance is above the impedance associated with the global node. Due to the depth-first ordering, these regions show up as uninterrupted intervals on the diagonal of the impedance matrix (Figure 1F). New nodes are then added as child nodes of the root node (c_0 to c_5 in Figure 1F), and each of

these child nodes integrates regions from within one uninterrupted interval. Next, for each of the child nodes, the impedance matrix is restricted to its associated regions (which now correspond to the dendritic subtrees; red squares in Figure 1G), and the procedure is repeated until we reach the maximal value of the impedance matrix, since at that point, the whole dendrite is covered.

To study interactions between a subset of input regions on the dendritic tree, the full NET is pruned (see STAR Methods) so that only nodes that integrate the regions of interest are retained (Figures 1H and 1I). Note that we employ two ways of visualizing the NET. When we plot the full NET associated with a neuron, we collapse all regions in a section without bifurcations onto a single line, so that the graphical structure mimics the original morphology (Figure 1H). When we prune the NET so that the set of regions is sufficiently small, we plot the full tree (Figure 1I). The vertical lengths of the branches leading up to the nodes are plotted proportional to the impedance associated with that node. This gives a visualization of how electrically close regions on the morphology are (as in the morpho-electric transform by Zador et al., 1995).

We illustrate how the dendritic voltage at these regions of interest is constructed by the NET. Each nodal voltage component is computed by convolving the impedance kernel at that node with all inputs to its subtree (Figure 1J). The local dendritic voltage at a location is then constructed by summing the NET voltage components of all nodes on the path from root to leaf (Figure 1K), so that the local voltage is indeed a superposition of both global and local components. Note that this local voltage coincides with the voltage computed through simulating an equivalent NEURON model (Carnevale and Hines, 2004) (dashed versus full line in Figure 1K). The key observation here is that the NET leafs (nodes $N = 1, 2, 3$) do not receive inputs from other locations (Figure 1J), in contrast to the local voltages in the biophysical model (Figure 1K). Furthermore, while in this example we have only implemented α -amino-3-hydroxy-5-methyl-4-isoxazolepropionic acid (AMPA) synapses, it is straightforward to use other voltage dependent currents (i.e., NMDA or voltage-gated ion channels).

In conclusion, by formulating the NET framework, we have solved the tangling problem. We have introduced voltage components at the NET leafs that only depend on local inputs while being able to accurately model synaptic interactions. To assess independence, we only have to quantify the influence of global NET components on the voltage-dependent factors in the local synaptic currents. After validating the NET framework, we will turn our attention to this question.

Validation of the NET Framework

We derived NETs for three vastly different exemplar morphologies (a cortical stellate cell [Wang et al., 2002], a granule cell [Carim-Todd et al., 2009], and a L5 cortical pyramidal cell [Hay et al., 2011]; Figures 2A–2C). We then reconstructed the impedance matrix of the NET (Figures 2A–2C, top right panels) and compared it with the exact impedance matrix. The small value of the root mean square error (RMSE) between both matrices suggests that the NET will accurately reproduce the full neuronal dynamics (Figure 2D). To ascertain this, we implemented a simu-

lation algorithm for the NET (see Methods S1), equipped each NET with somatic AP channels, and simulated it for 100 s while providing Poisson inputs to 100 randomly distributed excitatory and inhibitory synapses (see STAR Methods for all the simulation parameters). The resulting somatic voltage traces coincide with the traces obtained from equivalent NEURON simulations (Carnevale and Hines, 2004) (Figures 2A–2C, bottom right panels). Consequently, somatic RMSEs are low while spike prediction is excellent (Figure 2E). Thus, the RMSE between the true impedance matrix and its NET approximation is a good predictor of the accuracy of the NET. While here the synapse distribution was random, NETs are equally accurate when synapses are clustered (Figures S1D and S1E). Furthermore, intra-dendritic dynamics and regenerative NMDA events are well reproduced by NETs (Figures S1E and S1F).

A Single Number to Approximate the Degree of Independence between Regions

We have established that NET leafs only receive local inputs. These nodes hence only integrate local synaptic input currents (modeled as the product between synaptic conductance and voltage dependent factors $I_{\text{syn}}(t) \equiv g_{\text{syn}}(t)f(V(t))$, the latter representing for instance driving force and/or NMDA activation). As per the NET framework, the local dendritic voltage can be decomposed as

$$V(t) = \bar{V}_{\text{global}}(t) + \bar{V}_L(t), \quad (\text{Equation 1})$$

where $\bar{V}_L(t)$ is the leaf voltage component and $\bar{V}_{\text{global}}(t)$ is the sum of all other voltage components on the path from root to leaf (note that we denote NET-related quantities with a line over the variable). The leaf voltage is computed by convolving the synaptic input current with the impedance kernel $\bar{Z}_L(t)$ associated with the leaf node:

$$\bar{V}_L = \bar{Z}_L(t) * g_{\text{syn}}(t)f(\bar{V}_{\text{global}}(t) + \bar{V}_L(t)). \quad (\text{Equation 2})$$

From this equation, it can be seen that \bar{V}_L will be independent from all other synaptic inputs if the fluctuations in $\bar{V}_L(t)$ are large compared to the fluctuations in $\bar{V}_{\text{global}}(t)$. In such a case, regenerative events are elicited solely by reinforcing initial perturbations in $\bar{V}_L(t)$. Conversely, if the fluctuations in $\bar{V}_{\text{global}}(t)$ are sizeable compared to the fluctuations in $\bar{V}_L(t)$, there will be a large degree of cooperativity between the region that leaf L integrates and other regions.

We observe that voltage fluctuations at each node are approximately proportional to the associated nodal impedances (Figure 2F). Thus, we expect fluctuations in $\bar{V}_L(t)$ to be large compared to fluctuations in $\bar{V}_{\text{global}}(t)$ if the associated leaf impedance \bar{Z}_L is large compared to all other impedances on the path from root to leaf. When considering the mutual independence of a pair of regions, the root node of the pruned NET is the only node that integrates both inputs. Hence, for mutual independence, the impedances associated with each leaf node must be large compared to the impedance associated with the root node. We thus propose the “impedance-based independence

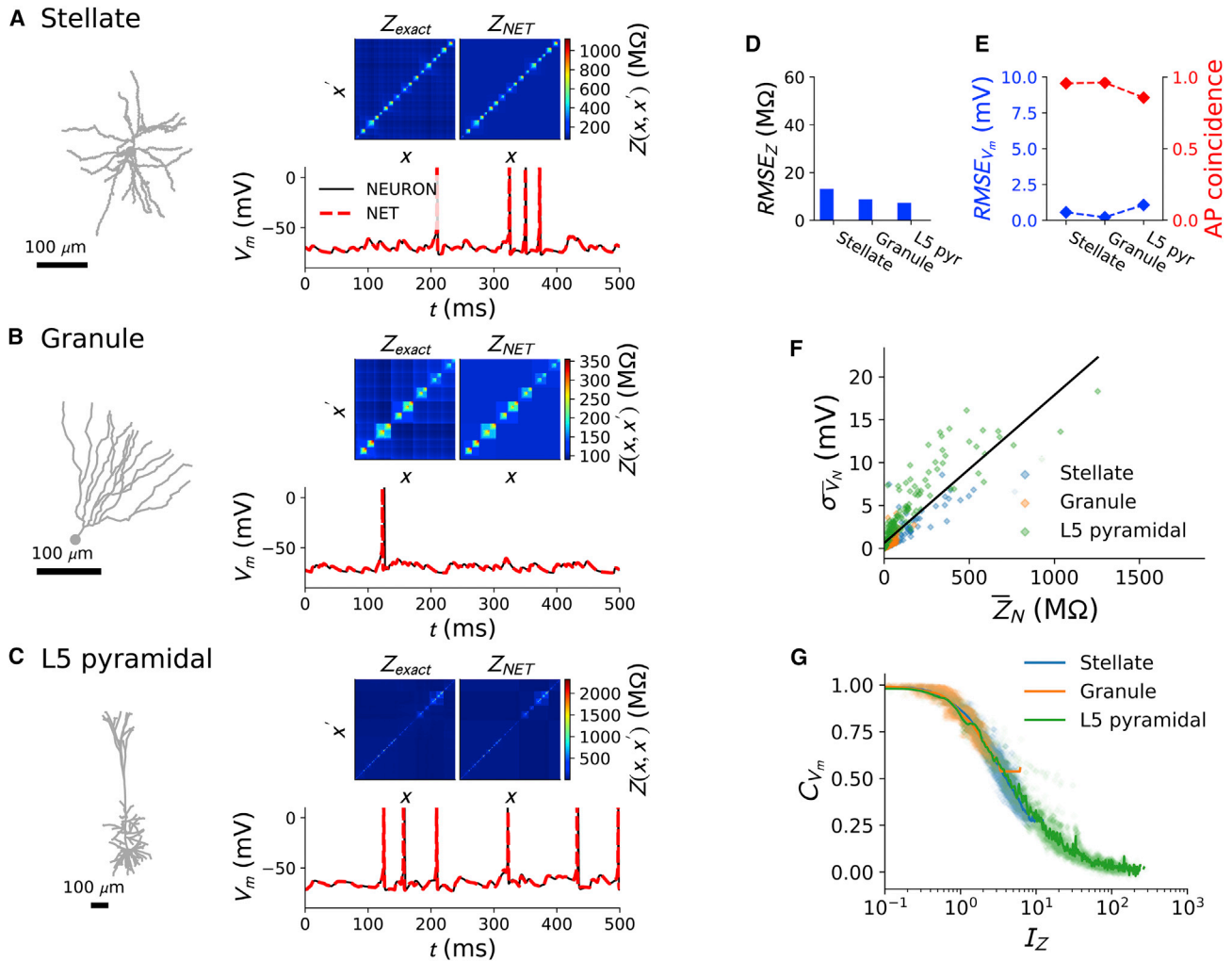


Figure 2. Validation of the NET Framework and the Impedance-Based Independence Index I_Z

- (A) Cortical stellate cell.
 (B) Hippocampal granule cell.
 (C) Cortical L5 pyramidal cell. For each cell, morphology is shown on the left, the exact impedance matrix and its NET approximation on the top right, and the somatic voltage traces from equivalent NET and NEURON simulations on the bottom right.
 (D) RMSE between NET and exact impedance matrices for each cell.
 (E) Subthreshold somatic voltage RMSE (blue) and spike coincidence factor (red).
 (F) Size of fluctuations of each nodal voltage component (quantified by its SD) as a function of the associated nodal impedance. The black line is a linear least-squares fit to the data.
 (G) Voltage correlation between each pair of synapses on the three cells as a function of I_Z . Lines are obtained from kernel regression.
 See also [Figure S1](#).

index” I_Z to quantify pairwise independence as the ratio of leaf over root impedance of the pruned NET:

$$I_Z = \frac{\bar{Z}_1 + \bar{Z}_2}{2\bar{Z}_R} \quad (\text{Equation 3})$$

We plotted the membrane voltage correlations between each pair of synapses on our exemplar cells, obtained from our validation simulations (Figures 2A–2C), as a function of I_Z . These correlations decrease uniformly as a function of I_Z (Figure 2G),

and the functional form of this decrease does not depend on the morphology. Consequently, across cell types, I_Z could be a good predictor of the degree of independence between regions. We then investigated a number of ways in which changes in morphological and electrical factors could influence membrane voltage correlations and found that their effect on these correlations can be summarized entirely by their effect on I_Z (Figures S2F–S2H).

To speak of mutual independence between pairs of regions, their layout needs to be somewhat symmetric, so that \bar{Z}_1 and \bar{Z}_2 do not differ too much. If region 1 would, for instance, be

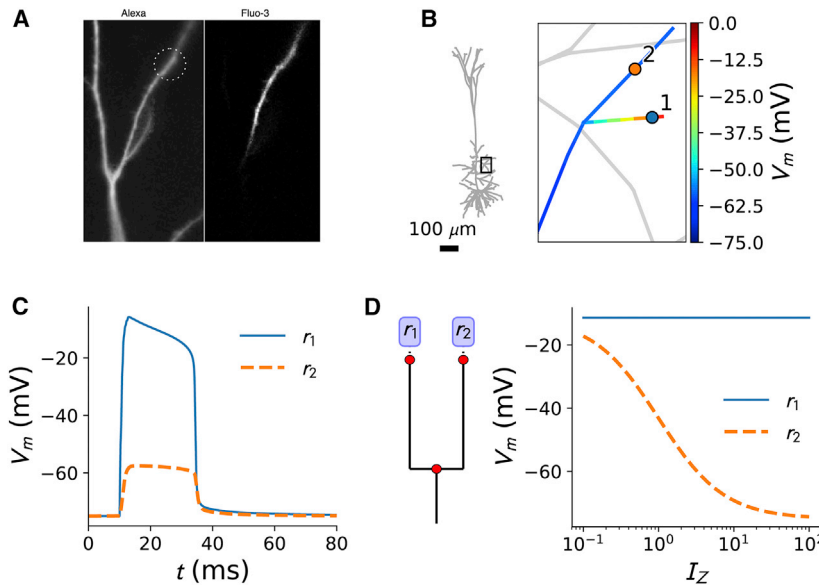


Figure 3. Voltage Attenuation Makes Dendritic Branches Look Highly Compartmentalized

(A) Example of a typical experimental situation. A branch is stimulated through two-photon glutamate uncaging (dashed circle, left), and a correlate of the voltage (here Ca^{2+} , right) is measured (adapted with permission from Wei et al., 2001).

(B) Spatial voltage (computed with NEURON) in an oblique apical fork 10 ms after supra-threshold stimulation of an NMDA synapse at region 1. A rapid decrease of the depolarization makes the branches seem highly compartmentalized. $I_Z = 3$ between regions 1 and 2.

(C) Trace of the depolarization at regions 1 and 2.

(D) Toy NET model, representing a dendritic fork, where I_Z could be varied at will (left). Depolarization at regions 1 and 2 is shown as a function of I_Z following an input to region 1 (right).

much closer to a bifurcation than region 2, so that $\bar{Z}_1 \ll \bar{Z}_2$, then a regenerative event at region 1 would propagate without much attenuation to region 2. Hence, it would be impossible to independently generate local spikes at region 2. On the other hand, regenerative events at region 2 would substantially attenuate to region 1, so that it might be possible to have independent regenerative events at region 1. Thus, mutual independence and I_Z are only meaningful if the regions lie in a somewhat symmetric configuration around the nearest bifurcation.

We have defined I_Z based on the NET framework. In the familiar terminology of input and transfer impedances, \bar{Z}_R corresponds to the transfer impedance Z_{12} between two regions, and the NET leaf impedances \bar{Z}_i ($i = 1, 2$) are related to the input impedances Z_i by $\bar{Z}_i = Z_i - Z_{12}$. Substituting this in Equation 3, we obtain:

$$I_Z = \frac{Z_1 + Z_2}{2Z_{12}} - 1. \quad (\text{Equation 4})$$

Thus, I_Z is nothing but the ratio of input over transfer impedance, shifted so that I_Z is zero when the regions are the same. I_Z is thus a measurable index and can be computed from experimental data or traditional biophysical models.

The Threshold for Independence

Correlations between regions on the dendrite decrease in a continuous fashion as a function of I_Z (Figure 2G). We nevertheless wondered whether it is possible to find a threshold I_Z above which regions constitute independent subunits (i.e., where local regenerative events are elicited independently from ongoing dynamics elsewhere).

Experimentally, the idea has emerged that every branch can be considered as an independent computational subunit (Branco and Häusser, 2010). Sharp drops in transfer impedance across bifurcation points may lead to this idea, as delivering relatively few stimuli to a single dendritic branch (for instance,

through two-photon glutamate uncaging; Petit et al., 1997) leads to a marked attenuation of the measured signal (typically Ca^{2+} dye luminescence or voltage) across bifurcation

points (Wei et al., 2001) (Figure 3A). Nevertheless, inferring the extent of the dendritic subunits in this way is somewhat problematic. First, the Ca^{2+} signal itself is thought to be more local than the voltage signal (Biess et al., 2011; Nevian and Sakmann, 2004; Simon and Llinás, 1985; Yuste and Denk, 1995) while also being influenced by the nonlinear activation function of voltage-dependent calcium channels (Almog and Korngreen, 2009). Second, even though there may be a relatively large amount of voltage attenuation across bifurcation points (Figures 3B and 3C), the remaining depolarization can still cause cooperativity between synapses during an ongoing barrage of inputs. To test this idea, we constructed a toy model with two leaves and one root representing, for instance, a single trunk that bifurcates into two child branches. This model allowed us to vary I_Z on a log scale between 0.1 and 100 (Figure 3D, left) by changing the ratio of leaf versus root impedance while keeping the total input impedance at each site constant. We then stimulated synapse 1 with a supra-threshold conductance (strong enough to elicit an NMDA spike) and measured the depolarization in branch 1 and branch 2. It can be seen that there is substantial voltage attenuation; at $I_Z = 1$, only 50% of the depolarization in branch 1 arrives at branch 2 (Figure 3D, right panel). Nevertheless, membrane voltage correlations decrease less as a function of I_Z , so that for $I_Z = 1$, this correlation is still close to 1 (Figure 2G).

We thus aim at constructing a criterion for independence between dendritic regions that is valid when the dendritic tree receives an ongoing barrage of input. To do so, we construct a control NET where the leaves are completely independent by replacing \bar{V}_{global} (Equation 2), the sum of all voltage components associated with nodes that integrated more than one region) in the synaptic currents by their long-term average (here computed as a 200 ms low-pass filter of the root voltage under Poisson stimulation with a fixed rate). Consequently, in this independent NET (iNET), leaf voltage components (and thus the synaptic currents) only depend on the local inputs by construction.

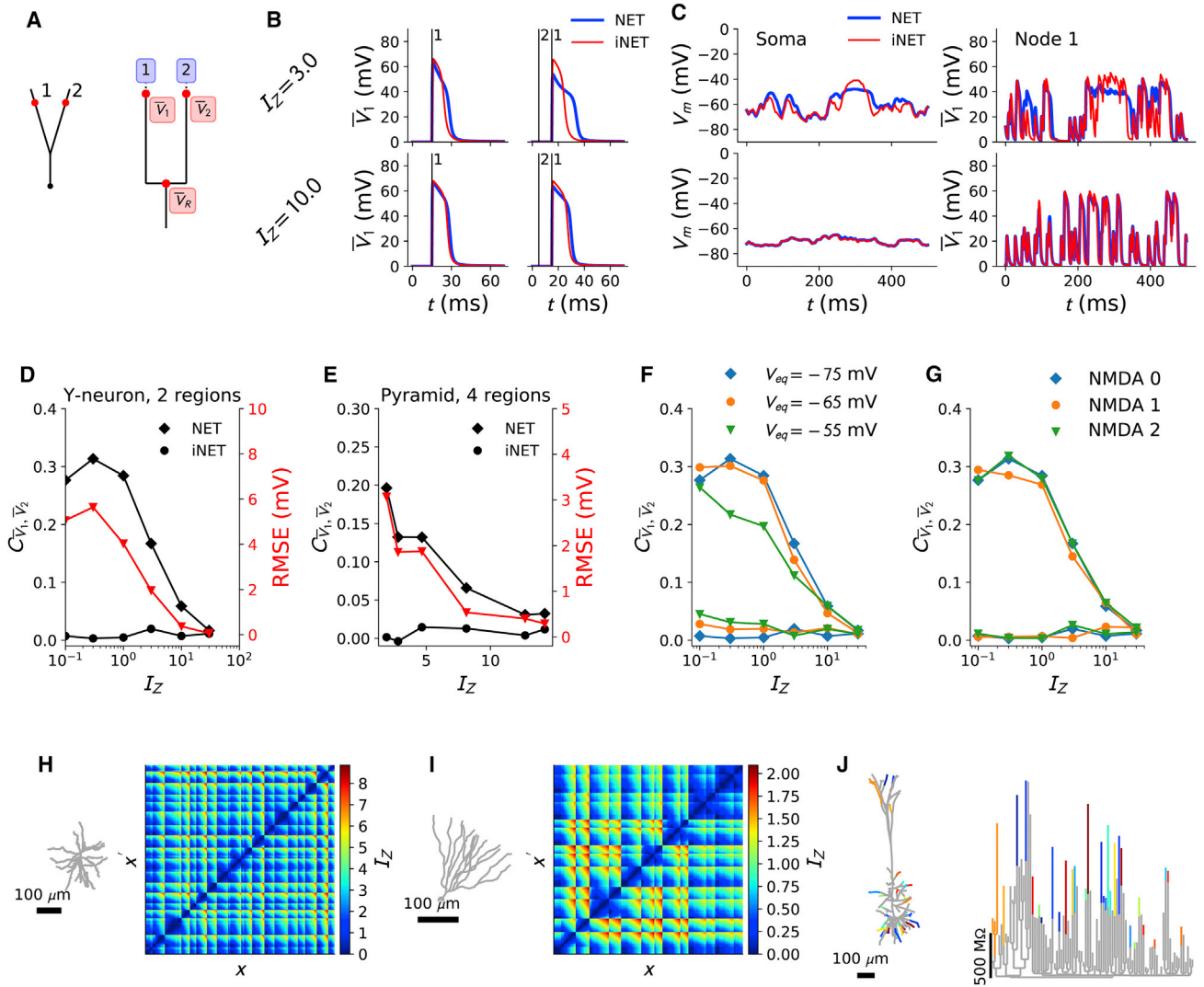


Figure 4. The Impedance-Based Independence Index I_Z Leads to a Systematic Characterization of Independent Subunits

(A) Toy model morphology and associated NET.
 (B) Voltage associated with leaf node 1 for $I_Z = 3$ (top) and $I_Z = 10$ (bottom). iNET (red) and NET (blue) traces for a single input to synapse 1 (left) and for inputs to synapses 1 and 2 (right). Vertical black lines indicate input arrival.
 (C) Same model, but now both synapses receive Poisson inputs. Somatic voltage (here equal to \bar{V}_R , left) and node voltage (right) are shown for $I_Z = 3$ (top) and $I_Z = 10$ (bottom).
 (D) The correlation between leaf voltage components of NET and iNET (black), and their somatic RMSE (red), as a function of I_Z . Same model as in (A)–(C).
 (E) Same as in (D), but with 4 inputs regions selected on the L5 pyramidal cell in each simulation. The x axis represents the average I_Z between regions.
 (F) Correlation between leaf voltage components of NET (decreasing line) and iNET (flat lines) for different equilibrium potentials. Same model as in (A)–(C).
 (G) Same as (F), but for different NMDA voltage dependences (0, STAR Methods Equation 9; 1, STAR Methods Equation 10; and 2, STAR Methods Equation 11)
 (H) Cortical stellate cell.
 (I) Hippocampal granule cell. For these cells, morphology is shown on the right and associated matrix of I_Z values on the left.
 (J) Cortical L5 pyramidal cell. Morphology (left) with color-coded independent regions at $I_Z \geq 10$ and NET with the same color-coded independent subunits (right). Note that individual compartments are always connected; color matches between separated compartments are accidental.
 See also Figures S2–S4.

Convergence between the iNET and the normal NET then indicates independence between input regions. We illustrate the iNET in a toy model with two leaves and one root (Figure 4A). When a synaptic input arrives at synapse 1, an NMDA event will be generated in branch 1. The leaf voltage associated with

this event is shown in the leftmost panels in Figure 4B. The effect of a strong input at synapse 2 on the dynamics in branch 1 depends on I_Z ; for $I_Z = 3$, the shape of the NET voltage trace at leaf 1 is drastically modified, whereas at $I_Z = 10$, there is little change (Figure 4B, rightmost panels). In the iNET, the traces at

leaf 1 with or without input to synapse 2 are identical by construction. Hence, when the dynamics of the NET converge to those of the iNET, the associated input regions constitute independent subunits. We stimulated both input sites with Poisson inputs, and at $l_z = 3$, the iNET voltage traces at soma and leaf deviate significantly from their NET counterparts (Figure 4C, top). The cooperative dynamics between input sites are thus nonnegligible. At $l_z = 10$, the iNET and NET dynamics agree very well (Figure 4C, bottom). Analyzing the correlations between both leaf voltage components confirms this finding; for $l_z \geq 10$, the NET correlation approaches the iNET value of zero (Figure 4D). The RMSE between the somatic traces also vanishes for $l_z \geq 10$. These results generalize to realistic neuron models and multiple input regions; analysis of leaf voltage correlations and somatic RMSEs for NETs obtained by distributing four input regions on the pyramidal cell morphology (Figure 2C) yields similar results (Figure 4E; x axis represents the average l_z between the input regions). Furthermore, these results are robust for different equilibrium potentials (Figure 4F) and different voltage dependencies of the NMDA current (Figure 4G). We thus conclude, as a rule of the thumb, that for $l_z \geq 10$, pairs of dendritic regions can be considered independent.

We then analyzed the asymptotic equilibrium points of the NMDA dynamics. With these points, the dynamic aspects of NMDA spikes can be fully understood (Major et al., 2008), as they represent the voltage a dendritic branch is trying to reach given the input to NMDA synapses. Nevertheless, influence of neighboring inputs on these points has never been investigated. We developed a method to compute these points for any input configuration (see Methods S1) and studied at which l_z values a fully developed NMDA spike can form independently in a branch (Figure S2B). We also asked at which l_z values two NMDA spikes would sum together, as they would for independent subunits (Figure S2C). Finally, we investigated the effective shift in potentiation threshold as a function of l_z (Figures S2D and S2E). These analyses corroborated our conclusion that, for $l_z \geq 10$ dendritic regions function as independent subunits.

A Formal Definition of Dendritic Compartmentalization

Next, we asked how many independent regions could maximally coexist along a dendritic tree, as well as what their location would be. We constructed an algorithm that divides the dendritic tree into regions separated by a minimal l_z (see STAR Methods). For the stellate and granule cells, we did not identify any compartments, as there were no l_z values greater than 10 in these cells (Figures 4H and 4I). In the pyramidal cell, the number of compartments for $l_z \geq 10$ was far less than the number of dendritic terminals (Figure 4J). Even at lower l_z values, there are still much fewer independent subunits than dendritic terminals (Figure S3; see, for instance, compartment numbers for $l_z \geq 3$). Note in this context that compartment numbers are fairly robust with respect to the biophysical parameters (Figure S4A); increasing axial resistance and membrane conductance, as well as adding a spine correction factor, increase compartment numbers slightly, whereas increasing the dendritic radii results in a moderate decrease of compartment numbers. We conclude that because cooperativity between synapses decreases less than voltage attenuation as a function of electrical separation, the

number of independent subunits that can coexist on a dendritic tree is lower than the number of dendritic branches. Our results thus contradict the notion that every branch constitutes an independent electrical subunit.

Comparison of the Model to the Electrical Properties of Basal Dendrites

In order to validate if the predicted l_z values, and thus the degree of electrical compartmentalization, are physiologically plausible, we reanalyzed dual dendritic patch-clamp recordings from the basal dendrites of neocortical L5 pyramidal neurons (Nevian et al., 2007). We computed l_z between dendritic branches with similar electrical properties emanating from the soma (Figure 5A). We corrected the recorded traces for experimental inaccuracies in access resistance compensation (Figure S5) and extracted steady-state responses during hyperpolarizing current pulses to infer input and transfer impedances (Figures 5B and 5C). Error bars on the input impedance values were determined from the accuracy of the access resistance fit to estimate the experimental variability (Figure S5C). The uncompensated recordings gave quantitatively similar results. We estimated l_z according to Equation 4 and found that the values agreed well with predictions from the L5 pyramidal cell model (Figure 5D). We consequently conclude that our predictions on compartment numbers (as long as the threshold of $l_z \geq 10$ predicted by the models is correct) are compatible with experimental data.

Dendritic Compartmentalization Can Be Modified Dynamically by Inputs

As neurons perform different input-output transformations at different moments in time, such as during up- and down-states (Wilson and Kawaguchi, 1996), we hypothesized that the number of compartments in dendrites can be modified dynamically by input patterns—an idea corroborated by recent experimental results (Cichon and Gan, 2015; Poleg-Polsky et al., 2018). In principle, shunting inputs could mediate such a change. Indeed, a voltage component with impedance kernel $Z(t)$, a shunting conductance g_{shunt} , and excitatory conductances g_e :

$$V = Z(t) * \left[-g_{\text{shunt}}V + \sum_e g_e f(V) \right] \quad (\text{Equation 5})$$

can be reinterpreted in the following way (see Methods S1):

$$V \approx \frac{Z(t)}{1 + Z(t) * g_{\text{shunt}}} * \left[\sum_e g_e f(V) \right], \quad (\text{Equation 6})$$

so that the shunt effectively reduces impedance (note that this relation is approximate, since, by rewriting Equation 5 in this way, we took V in the shunt term out of the convolution). When shunts are placed on the dendrite in such a way that they primarily affect shared nodes, independence between branches would increase.

In the high-conductance state (Destexhe et al., 2003), a state occurring *in vivo* when many synapses are randomly activated, the conductance of the membrane is increased over the whole

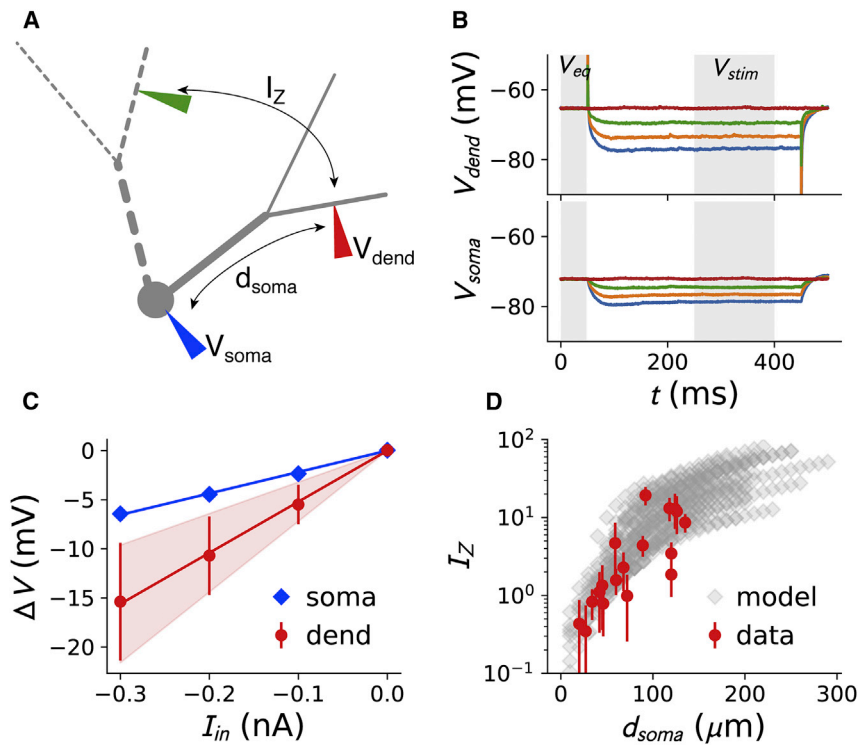


Figure 5. Estimating I_Z from Dendritic Patch-Clamp Data

(A) Schematic depiction of the analysis. Input and transfer (both dendrite to soma and soma to dendrite) impedance values were estimated from simultaneous dendritic and somatic voltage recordings. Input current steps were either injected at the dendritic or the somatic electrode. The extracted impedances were then used to compute what I_Z would be between the dendritic electrode site and a site at equal distance from the soma on a hypothetical dendritic branch with similar electrical properties.

(B) Example voltage response traces. Voltage difference was computed as $\Delta V = V_{stim} - V_{eq}$, where V_{stim} is the average access-resistance-corrected voltage between 200 and 350 ms after stimulus onset and V_{eq} is the average voltage in the 50 ms before onset.

(C) Impedance values were extracted from the slope of the regression line between input current (here delivered at the dendritic electrode) and ΔV (data extracted from traces shown in B). Error bars were determined from the access resistance fit (Figure S5).

(D) I_Z as a function of the distance of the dendritic electrode to the soma (red, experimental data; gray, L5 pyramidal cell). See also Figure S5.

dendritic tree, implementing a global shunt. A priori, two things could happen: either the root impedance of the associated NET could decrease more than the leaf impedances, in which case the number of subunits would increase, or the root impedance could decrease less than the leaf impedances, in which case the number of subunits would decrease. Because the root node of the associated NET integrates much more inputs than more local nodes, the former tends to decrease more than the latter. We illustrate this effect in the stellate cell, where a NET was derived for three input locations (Figure 6A): once at rest (Figure 6B, black NET) and once in the high conductance state (Figure 6B, blue NET, computed by adding the time-average conductance of the background synapses to the membrane as static shunts). Because root impedance decreases more than leaf impedance, electrical separation becomes stronger between branches that only have the root in common, and compartments emerge in the stellate cell (Figure 6C). The high-conductance NET is accurate in reproducing the average voltages; traces in Figure 6D (full colored lines) agree very well with the average post-synaptic potentials computed during an ongoing barrage of balanced excitation and inhibition (dashed colored lines).

Since both theory (Gidon and Segev, 2012) and connectivity data (Bloss et al., 2016) suggest the importance of the precise location of synaptic inhibition, we investigate the influence of precisely located inhibitory inputs on compartmentalization. In the apical tree of the L5 pyramidal neuron (Figure 6E), we noticed that the sibling branches in a particular apical fork did not constitute separate compartments (locations 3 and 4 in Figure 6F). Upon inserting inhibitory synapses near the branch point between the two terminal segments, they separate into indepen-

dent subunits (Figure 6F, bottom). The required inhibition (with a time-averaged conductance of 5 nS) could be provided by the somatostatin-positive interneuron pathways targeting the apical tuft (Markram et al., 2015; Muñoz et al., 2017). This change in compartmentalization can be quantified by the change in I_Z (Figure 6H). Note that the effect is location specific; independence between locations 1 and 2 does not increase. We performed simulations where each synapse pair received Poisson inputs (Figure 6G; note that NET traces again agree with the NEURON simulation) and computed the correlations between both pairs of synapses (Figure 6I). The decrease in correlation upon activation of the shunting inhibition is consistent with the reduction in I_Z .

Dynamic Compartmentalization Can Enable Branch-Specific Learning

Recent experiments have demonstrated that inhibitory interneurons are required for branch-specific plasticity (Cichon and Gan, 2015). Can a transient re-compartmentalization, mediated by inhibition, underlie this branch-specific learning? Before learning, post-synaptic targeting is thought to be unspecific (Gerstner et al., 1996). Hence, inputs coding different stimulus features can arrive at the same branch, but with different strengths. We ask whether sibling branches in the apical tree of the L5 pyramidal neuron (Figure 7A) can learn to become selective only to the strongest initial feature (Figure 7A) using only NMDA spikes and no APs (Hardie and Spruston, 2009). If two branches receive different synaptic activation (quantified as the product between input impedance and synaptic conductance), then the voltage difference between these branches will be larger when they are separated by a higher I_Z (Figure 7B), and therefore the probability

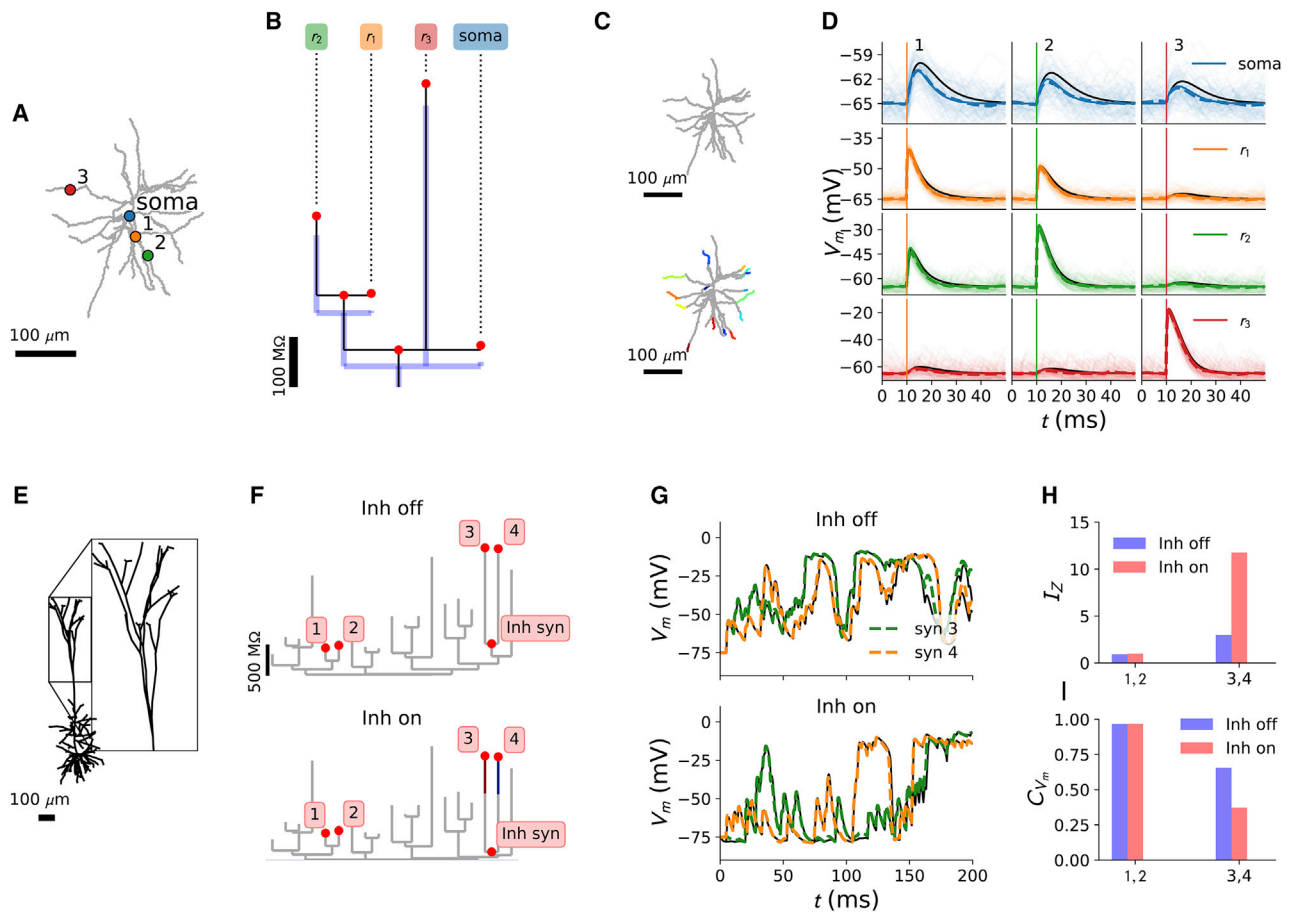


Figure 6. Dynamic Compartmentalization due to Spatiotemporal Input Patterns

(A) Stellate cell morphology with three input regions (numbers 1–3) and somatic readout.
 (B) NET for the configuration in (A) at rest (black) and in the high-conductance state (blue).
 (C) Compartmentalization for $I_Z \geq 10$ in the rest state (top) versus the high-conductance state (bottom).
 (D) At the three regions of interest, a strong excitatory synapse was inserted. The average post-synaptic potential was computed over 100 trials (dashed line) and coincides with the NET prediction (full line). Responses without background activity are plotted in black for reference.
 (E) Apical tuft of the L5 pyramidal cell, where we studied the effect of inhibition on the compartmentalization.
 (F) NET associated with the apical tuft, without (top) and with (bottom) inhibition (with an time-averaged conductance of 5 nS).
 (G) Voltage traces at synapses 3 and 4 without (top) and with (bottom) shunting inhibition (black trace is the equivalent NEURON simulation).
 (H and I) I_Z change when inhibition is turned on (H), and associated change in membrane correlation when synapses in both branches were stimulated with random Poisson trains (I).

increases to robustly potentiate the preferred branch while the nonpreferred branch is depressed. For the selected branches, activation of inhibitory synapses near the bifurcation point increased I_Z from 3.0 to 8.5 (Figure 7C, black versus blue tree). The original I_Z value was too low (Figures 7D and 7G), resulting in a positively correlated weight evolution in the preferred and nonpreferred branches (Figure 7F). Activation of inhibitory synapses near the bifurcation point increased I_Z , thus anticorrelating the weight evolution (Figure 7F) and enabling branch-specific learning (Figures 7E and 7G).

DISCUSSION

In this work, we formalized electrical dendritic compartmentalization. We have shown that dendritic regions are independent

if the fluctuations in global NET voltage components are small compared to the fluctuations in local NET voltage components. Furthermore, the relative sizes of these fluctuations are tightly related to the sizes of the associated NET impedances. We have thus proposed I_Z as a ratio of these impedances and have shown that this number is a good and measurable predictor of independence. We found that for $I_Z \geq 10$, pairs of dendritic sites function as independent subunits. Furthermore, we have used the NET to design an algorithm that, given a threshold I_Z , yields the maximal number of regions that can coexist on the dendritic tree separated by at least this threshold I_Z .

We have then performed this analysis on a number of cell classes (Figure S3) and found, in line with another recent study (Ujfalussy et al., 2018), that many branches are not separated by I_Z values required for independence. Impedance drops across

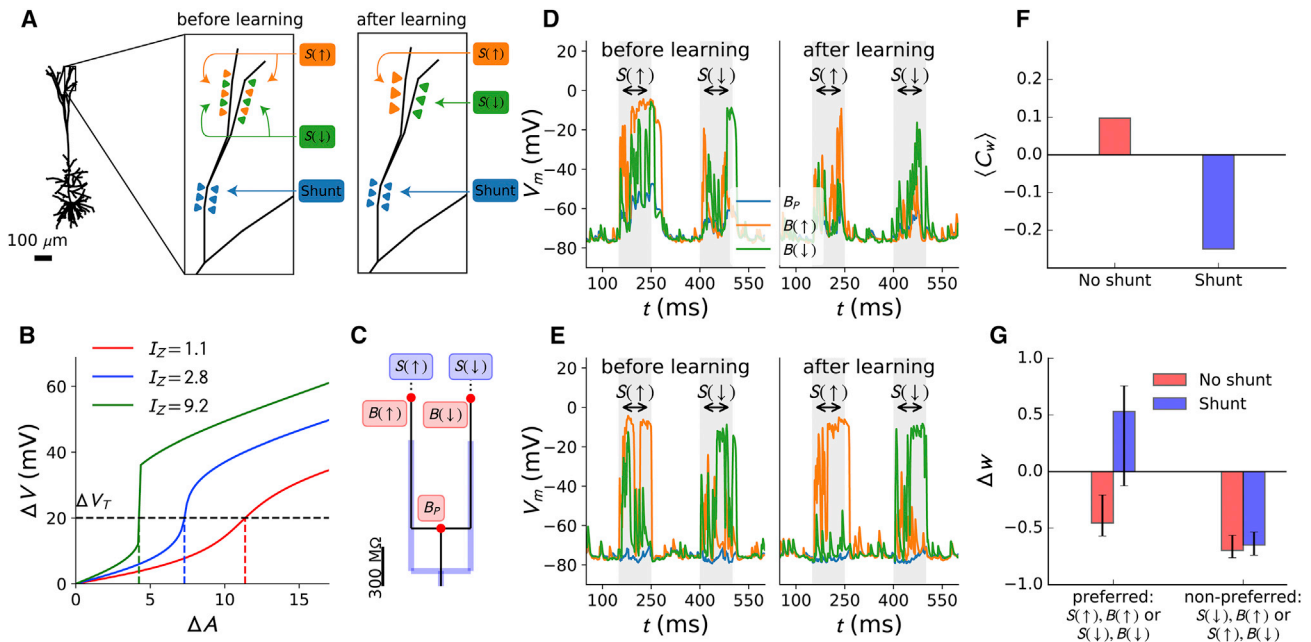


Figure 7. Enabling Branch-Specific Learning with Shunting Conductances

(A) Sketch of the situation. Before learning, two sibling branches are both targeted by synapses coding for either an up stimulus $S(\uparrow)$ (orange) or a down stimulus $S(\downarrow)$ (green). One branch $B(\uparrow)$ receives more synapses of the former stimulus, and the other branch $B(\downarrow)$ receives more of the latter stimulus. Branches should learn to be sensitive only to the stimulus that was initially the most prevalent (the “preferred” stimulus).
 (B) Difference in voltage across sibling branches ΔV increases as a function of the difference in activation ΔA . For higher I_Z , this increase is steeper. Consequently, a given threshold ΔV (black dashed line) is reached for lower ΔA (colored vertical lines).
 (C) Schematic of the NET without (black) and with (blue) shunt.
 (D and E) The learning task without (D; effective $I_Z = 3.0$) or with (E; effective $I_Z = 8.5$) shunting inhibition. For each epoch, both stimuli are presented for 100 ms, with 150-ms intervals in between them, for a total of 20 epochs. The initial and final epochs are shown.
 (F) Correlation between the average weights of the synapses in the preferred and nonpreferred branches during stimulus presentation, averaged over all epochs and 20 repetitions of the learning task.
 (G) Bar plot of the weight difference after the final epoch for all repetitions of the learning task. The bar lengths denote the medians of the weight difference distributions and the error bars the 25–75 percentiles.

dendritic bifurcations lead to large voltage attenuation (Figure 3), and studying simple input scenarios may lead to the idea that sibling branches automatically constitute independent subunits. However, in realistic scenarios where both branches receive an ongoing barrage of inputs, small transfer impedance values still lead to a large degree of cooperativity between synapses (Figure 4). Only for large electrical separations ($I_Z \geq 10$) are branches able to function independently. Although it is striking that a simple ratio of impedances can predict whether responses will be independent, earlier work has already hinted at the importance of impedances to explain dendritic response properties (Vetter et al., 2001).

Experimental data on the electrical coupling in fine dendritic branches, as required to support our theoretical findings, are rare. Nevertheless, we wondered whether our predictions could be validated. We found that existing recordings from fine basal dendrites of L5 pyramidal neurons in the neocortex allowed for the estimation of I_Z between different main branches emanating from the soma (Figure 5). The values we extracted agreed well with predictions by our model, thus validating that the latter lie within a biologically plausible range and confirming our predictions on compartmentalization. Ideally, to directly validate

our prediction of the relation between compartmentalization and I_Z , triple dendritic recordings of parent and higher-order daughter branches would have to be combined with the focal synaptic uncaging of glutamate to elicit local NMDA spikes or other regenerative events. A related approach would be to perform dual dendritic recordings *in vivo* to determine dendritic independence in the most natural state, yet these experiments are challenging and have not been performed so far.

We focused on electrical compartmentalization of dendrites and not on chemical compartmentalization. The latter might be more localized than the former, a classical example being the localization of Ca^{2+} signals within the spine head but not the neighboring dendrite (Nevian and Sakmann, 2004; Yuste and Denk, 1995). Stronger chemical compartmentalization may lead to localized plasticity (Govindarajan et al., 2011; Losonczy et al., 2008; Weber et al., 2016) and small spine cluster sizes (Frank et al., 2018; Fu et al., 2012; Gökçe et al., 2016) that could not be explained by electrical compartmentalization alone.

The heterogeneity of brain states (Wilson and Kawaguchi, 1996) and the observation that the electrical length of nerve fibers changes with the amount of background conductance (Segev and London, 2000) led us to explore the possibility that the

NET, and hence independence, could be modified dynamically by spatiotemporal input patterns. Up states (Destexhe et al., 2007) can increase membrane conductance across the neuron, as shown by simultaneous dendritic and somatic recordings *in vivo* (Waters and Helmchen, 2004). In such cases, the impedance associated with the root node of the NET decreases more compared to impedances associated with leaf nodes. This suggests that independence across branches increases during up states (Figures 6A–6D). Nevertheless, previous work on the dynamics in dendrites during such states (Farinella et al., 2014; Rudolph and Destexhe, 2003) suggests that in certain cases, it becomes easier to elicit dendritic regenerative events and also that the set of synapses required to trigger such an event can be more spatially distributed. This apparent paradox is resolved by realizing that branches can only act independently if the fluctuations in the global voltage component are small compared to fluctuations in the local voltage components (Equation 2). A synaptic bombardment during the high-conductance state has two effects: the increased synaptic conductance dampens fluctuations in the global voltage components, decoupling dendritic regions, and random noise increases these fluctuations, coupling dendritic regions. The final picture thus depends on the balance between these two effects, which may change according to brain state, region, and even across different regions on the same cell.

The interaction of inhibition with NMDA spikes has been studied extensively. It is now known that inhibition is well suited to veto NMDA-spike generation (Gidon and Segev, 2012; Rhodes, 2006), and allows for rapid switching between the on and off states of the NMDA plateau (Doron et al., 2017). Our work adds yet a third interaction to the repertoire, where inhibition (located near dendritic bifurcations) can decouple NMDA-spike generation in neighboring branches in a highly localized fashion, resulting in a precise tuning of compartmentalization (Figures 6E–6H).

How many branches on the dendritic tree lie within the useful range for dynamic re-compartmentalization? In pyramidal cells, compartments numbers doubled for values of I_Z between 3 and 10, and in smaller cells, these numbers increase 5-fold (Figure S3). This suggests that global conductance input increases the number of compartments 2- to 5-fold, depending on the cell's properties. Inspecting pairwise independence, we determine that in pyramidal cells, 5% to 10% of terminal pairs are separated by I_Z values between 3 and 10 (mainly terminals on the same main branches). In smaller cells, up to 60% of pairs fall within these values. On average, these pairs are made independent by shunting conductances of 5 to 15 nS (Figure S3).

To explore the functional consequences of dynamic compartmentalization, we equipped synapses on dendritic sibling branches with a voltage-based plasticity rule (Clopath et al., 2010) and explored whether these synapses could learn independently. Consistent with our prior observations, we found that a value of $I_Z \approx 3$ was too small for these branches to learn independently. Nevertheless, shunting inhibition that increased I_Z to 8.5 allowed the synaptic weights in both branches to evolve in an independent fashion. Interestingly, recent data suggest such phenomena may occur *in vivo* (Cichon and Gan, 2015).

Thus, the computation a neuron is engaged in may vary across brain states; when background conductance is high, neurons may prioritize in local dendritic learning, whereas otherwise, they may favor associative output generation.

The NET framework relies on two approximations: that impedance kernels with similar magnitudes share similar time-scales, so that they can be averaged, and that centripetal voltage attenuation is small compared to centrifugal attenuation (Nevian et al., 2007). We found these approximations to be true in all cortical neuron types we modeled. Furthermore, the NET framework is not restricted to the currents we modeled; Ca-spike generating channels can be included as well (Larkum et al., 1999). NETs express the interaction of a (sub)set of synapses in a background determined by the electrical properties of a morphology. Hence, there is freedom in choosing which synapses to model explicitly and which synapses to treat as background by including their average effect in the NET. This choice depends on the problem at hand. For instance, we have shown here that modeling shunting inhibition implicitly yields insight in the change in interaction between NMDA synapses.

Finally, we have devised an efficient inversion algorithm (see Methods S1), so that performant NET simulations can be designed. While for full neuron models, the standard simulation tools remain the preferable option (Carnevale and Hines, 2004), the NET framework allows for the definition of abstract dendrite models so that hallmark dendritic computations can be implemented in a minimal fashion. NETs may thus prove useful to scientists exploring the effects of dendrites at the network level.

Across the brain, neurons take on a wide variety of morphologies. We have shown here how these dendritic trees compartmentalize at rest and during dynamic input regimes. The behavioral relevance of up states (Destexhe et al., 2007), the specificity of inhibitory targeting (Bloss et al., 2016), and the importance of interneuron activity for branch-specific learning (Cichon and Gan, 2015) suggest that dynamic compartmentalization is ubiquitous in normal brain function, with far-reaching consequences for memory formation (Kastellakis et al., 2016) and capacity (Poirazi and Mel, 2001). Taken together, the NET can be seen as a computational description of the morphological neuron, complementary to the well-known biophysical description, and the algorithm to derive it as a translation from biophysics to computation.

STAR★METHODS

Detailed methods are provided in the online version of this paper and include the following:

- KEY RESOURCES TABLE
- CONTACT FOR REAGENT AND RESOURCE SHARING
- METHOD DETAILS
 - Biophysical modeling
 - Neural Evaluation tree
 - Independence and compartmentalization
 - Extracting I_Z from patch-clamp data
 - Simulation-specific parameters
- DATA AND SOFTWARE AVAILABILITY

SUPPLEMENTAL INFORMATION

Supplemental Information includes five figures and Supplemental Methods and can be found with this article online at <https://doi.org/10.1016/j.celrep.2019.01.074>.

ACKNOWLEDGMENTS

Funding was received from the ETH Domain for the Blue Brain Project (BBP) and the European Union Seventh Framework Program (FP7/2007-2013) under grant agreements FP7-26992115 (BrainScaleS) and FP7-604102 (The Human Brain Project), as well as EU grant agreement 720270 (HBP SGA1). We thank Profs. Idan Segev and Wulfram Gerstner and Dr. Arnd Roth for helpful advice and discussions and Drs. Luc Guyot, Jakob Jordan, and Aditya Gilra for proof-reading the manuscript.

AUTHOR CONTRIBUTIONS

W.A.M.W. and B.T.-N. designed the research. W.A.M.W. performed the mathematical modeling, implemented the models, and ran the simulations. W.A.M.W., B.T.-N., T.N., and M.-O.G. analyzed the results and wrote the paper.

DECLARATION OF INTERESTS

The authors declare no competing interests.

Received: June 20, 2018

Revised: October 3, 2018

Accepted: January 17, 2019

Published: February 12, 2019

REFERENCES

- Almog, M., and Korngreen, A. (2009). Characterization of voltage-gated Ca(2+) conductances in layer 5 neocortical pyramidal neurons from rats. *PLoS ONE* 4, e4841.
- Anderson, J.S., Carandini, M., and Ferster, D. (2000). Orientation tuning of input conductance, excitation, and inhibition in cat primary visual cortex. *J. Neurophysiol.* 84, 909–926.
- Ascoli, G.A. (2006). Mobilizing the base of neuroscience data: the case of neuronal morphologies. *Nat. Rev. Neurosci.* 7, 318–324.
- Behabadi, B.F., and Mel, B.W. (2014). Mechanisms underlying subunit independence in pyramidal neuron dendrites. *Proc. Natl. Acad. Sci. USA* 111, 498–503.
- Biess, A., Korkotian, E., and Holcman, D. (2011). Barriers to diffusion in dendrites and estimation of calcium spread following synaptic inputs. *PLoS Comput. Biol.* 7, e1002182.
- Bloss, E.B., Cembrowski, M.S., Karsh, B., Colonell, J., Fetter, R.D., and Spruston, N. (2016). Structured dendritic inhibition supports branch-selective integration in CA1 pyramidal cells. *Neuron* 89, 1016–1030.
- Bono, J., and Clopath, C. (2017). Modeling somatic and dendritic spike mediated plasticity at the single neuron and network level. *Nat. Commun.* 8, 706.
- Branco, T., and Häusser, M. (2010). The single dendritic branch as a fundamental functional unit in the nervous system. *Curr. Opin. Neurobiol.* 20, 494–502.
- Brette, R., and Destexhe, A. (2012). Intracellular recording. In *Handbook of Neural Activity Measurement*, R. Brette (Cambridge University Press), pp. 44–91.
- Carim-Todd, L., Bath, K.G., Fulgenzi, G., Yanpallewar, S., Jing, D., Barrick, C.A., Becker, J., Buckley, H., Dorsey, S.G., Lee, F.S., and Tessarollo, L. (2009). Endogenous truncated TrkB.T1 receptor regulates neuronal complexity and TrkB kinase receptor function in vivo. *J. Neurosci.* 29, 678–685.
- Carnevale, N.T., and Hines, M.L. (2004). *The NEURON Book* (Cambridge University Press).
- Chua, Y., and Morrison, A. (2016). Effects of calcium spikes in the layer 5 pyramidal neuron on coincidence detection and activity propagation. *Front. Comput. Neurosci.* 10, 76.
- Cichon, J., and Gan, W.-B. (2015). Branch-specific dendritic Ca(2+) spikes cause persistent synaptic plasticity. *Nature* 520, 180–185.
- Clopath, C., Büsing, L., Vasilaki, E., and Gerstner, W. (2010). Connectivity reflects coding: a model of voltage-based STDP with homeostasis. *Nat. Neurosci.* 13, 344–352.
- Cuntz, H., Forstner, F., Borst, A., and Häusser, M. (2010). One rule to grow them all: a general theory of neuronal branching and its practical application. *PLoS Comput. Biol.* 6, e1000877.
- De Sa, V.R., and MacKay, D.J.C. (2001). Model fitting as an aid to bridge balancing in neuronal recording. *Neurocomputing* 38–40, 1651–1656.
- Delon, J., Desolneux, A., Lisani, J.L., and Petro, A.B. (2007). A nonparametric approach for histogram segmentation. *IEEE Trans. Image Process.* 16, 253–261.
- Destexhe, A., Rudolph, M., and Paré, D. (2003). The high-conductance state of neocortical neurons in vivo. *Nat. Rev. Neurosci.* 4, 739–751.
- Destexhe, A., Hughes, S.W., Rudolph, M., and Crunelli, V. (2007). Are corticothalamic ‘up’ states fragments of wakefulness? *Trends Neurosci.* 30, 334–342.
- Doron, M., Chindemi, G., Muller, E., Markram, H., and Segev, I. (2017). Timed synaptic inhibition shapes NMDA spikes, influencing local dendritic processing and global I/O properties of cortical neurons. *Cell Rep.* 21, 1550–1561.
- Farinella, M., Ruedt, D.T., Gleeson, P., Lanore, F., and Silver, R.A. (2014). Glutamate-bound NMDARs arising from in vivo-like network activity extend spatio-temporal integration in a L5 cortical pyramidal cell model. *PLoS Comput. Biol.* 10, e1003590.
- Frank, A.C., Huang, S., Zhou, M., Gdalyahu, A., Kastellakis, G., Silva, T.K., Lu, E., Wen, X., Poirazi, P., Trachtenberg, J.T., and Silva, A.J. (2018). Hotspots of dendritic spine turnover facilitate clustered spine addition and learning and memory. *Nat. Commun.* 9, 422.
- Fu, M., Yu, X., Lu, J., and Zuo, Y. (2012). Repetitive motor learning induces coordinated formation of clustered dendritic spines in vivo. *Nature* 483, 92–95.
- Gerstner, W., Kempter, R., van Hemmen J.L., and Wagner, H. (1996). A neuronal learning rule for sub-millisecond temporal coding. *Nature* 383, 76–81.
- Gidon, A., and Segev, I. (2012). Principles governing the operation of synaptic inhibition in dendrites. *Neuron* 75, 330–341.
- Gökçe, O., Bonhoeffer, T., and Scheuss, V. (2016). Clusters of synaptic inputs on dendrites of layer 5 pyramidal cells in mouse visual cortex. *eLife* 5, e09222.
- Golding, N.L., Staff, N.P., and Spruston, N. (2002). Dendritic spikes as a mechanism for cooperative long-term potentiation. *Nature* 418, 326–331.
- Govindarajan, A., Israely, I., Huang, S.-Y., and Tonegawa, S. (2011). The dendritic branch is the preferred integrative unit for protein synthesis-dependent LTP. *Neuron* 69, 132–146.
- Grienberger, C., Chen, X., and Konnerth, A. (2015). Dendritic function in vivo. *Trends Neurosci.* 38, 45–54.
- Guerguiev, J., Lillicrap, T.P., and Richards, B.A. (2017). Towards deep learning with segregated dendrites. *eLife* 6, e22901.
- Hardie, J., and Spruston, N. (2009). Synaptic depolarization is more effective than back-propagating action potentials during induction of associative long-term potentiation in hippocampal pyramidal neurons. *J. Neurosci.* 29, 3233–3241.
- Hay, E., Hill, S., Schürmann, F., Markram, H., and Segev, I. (2011). Models of neocortical layer 5b pyramidal cells capturing a wide range of dendritic and perisomatic active properties. *PLoS Comput. Biol.* 7, e1002107.
- Hines, M.L., Morse, T., Migliore, M., Carnevale, N.T., and Shepherd, G.M. (2004). ModelDB: a database to support computational neuroscience. *J. Comput. Neurosci.* 17, 7–11.
- Jack, J.J., Noble, D., and Tsien, R.W. (1975). *Electric Current Flow in Excitable Cells* (Clarendon Press Oxford).

- Jahr, C.E., and Stevens, C.F. (1990a). A quantitative description of NMDA receptor-channel kinetic behavior. *J. Neurosci.* *10*, 1830–1837.
- Jahr, C.E., and Stevens, C.F. (1990b). Voltage dependence of NMDA-activated macroscopic conductances predicted by single-channel kinetics. *J. Neurosci.* *10*, 3178–3182.
- Johanning, F.W., Beed, P.S., Trimbuch, T., Bendels, M.H.K., Winterer, J., and Schmitz, D. (2009). Dendritic compartment and neuronal output mode determine pathway-specific long-term potentiation in the piriform cortex. *J. Neurosci.* *29*, 13649–13661.
- Kastellakis, G., Silva, A.J., and Poirazi, P. (2016). Linking memories across time via neuronal and dendritic overlaps in model neurons with active dendrites. *Cell Rep.* *17*, 1491–1504.
- Koch, C. (1998). *Biophysics of Computation: Information Processing in Single Neurons* (Computational Neuroscience) (Oxford University Press).
- Koch, C., Poggio, T., and Torre, V. (1982). Retinal ganglion cells: a functional interpretation of dendritic morphology. *Philos. Trans. R. Soc. Lond. B Biol. Sci.* *298*, 227–263.
- Koch, C., Poggio, T., and Torre, V. (1983). Nonlinear interactions in a dendritic tree: localization, timing, and role in information processing. *Proc. Natl. Acad. Sci. USA* *80*, 2799–2802.
- Koch, C., Douglas, R., and Wehmeier, U. (1990). Visibility of synaptically induced conductance changes: theory and simulations of anatomically characterized cortical pyramidal cells. *J. Neurosci.* *10*, 1728–1744.
- Larkum, M.E., and Nevian, T. (2008). Synaptic clustering by dendritic signalling mechanisms. *Curr. Opin. Neurobiol.* *18*, 321–331.
- Larkum, M.E., Zhu, J.J., and Sakmann, B. (1999). A new cellular mechanism for coupling inputs arriving at different cortical layers. *Nature* *398*, 338–341.
- Lavzin, M., Rapoport, S., Polsky, A., Garion, L., and Schiller, J. (2012). Nonlinear dendritic processing determines angular tuning of barrel cortex neurons in vivo. *Nature* *490*, 397–401.
- Lee, W.-C.A., Bonin, V., Reed, M., Graham, B.J., Hood, G., Glattfelder, K., and Reid, R.C. (2016). Anatomy and function of an excitatory network in the visual cortex. *Nature* *532*, 370–374.
- London, M., and Häusser, M. (2005). Dendritic computation. *Annu. Rev. Neurosci.* *28*, 503–532.
- Losonczy, A., Makara, J.K., and Magee, J.C. (2008). Compartmentalized dendritic plasticity and input feature storage in neurons. *Nature* *452*, 436–441.
- MacDonald, J.F., and Wojtowicz, J.M. (1982). The effects of L-glutamate and its analogues upon the membrane conductance of central murine neurones in culture. *Can. J. Physiol. Pharmacol.* *60*, 282–296.
- Major, G., and Evans, J.D. (1994). Solutions for transients in arbitrarily branching cables: IV. Nonuniform electrical parameters. *Biophys. J.* *66*, 615–633.
- Major, G., Evans, J.D., and Jack, J.J. (1993). Solutions for transients in arbitrarily branching cables: I. Voltage recording with a somatic shunt. *Biophys. J.* *65*, 423–449.
- Major, G., Polsky, A., Denk, W., Schiller, J., and Tank, D.W. (2008). Spatiotemporally graded NMDA spike/plateau potentials in basal dendrites of neocortical pyramidal neurons. *J. Neurophysiol.* *99*, 2584–2601.
- Major, G., Larkum, M.E., and Schiller, J. (2013). Active properties of neocortical pyramidal neuron dendrites. *Annu. Rev. Neurosci.* *36*, 1–24.
- Markram, H., Müller, E., Ramaswamy, S., Reimann, M.W., Abdellah, M., Sanchez, C.A., Ailamaki, A., Alonso-Nanclares, L., Antille, N., Arsever, S., et al. (2015). Reconstruction and simulation of neocortical microcircuitry. *Cell* *163*, 456–492.
- Mel, B.W., Ruderman, D.L., and Archie, K.A. (1998). Translation-invariant orientation tuning in visual “complex” cells could derive from intradendritic computations. *J. Neurosci.* *18*, 4325–4334.
- Moore, J.J., Ravassard, P.M., Ho, D., Acharya, L., Kees, A.L., Vuong, C., and Mehta, M.R. (2017). Dynamics of cortical dendritic membrane potential and spikes in freely behaving rats. *Science* *355*, 1–38.
- Muñoz, W., Tremblay, R., Levenstein, D., and Rudy, B. (2017). Layer-specific modulation of neocortical dendritic inhibition during active wakefulness. *Science* *355*, 954–959.
- Nevian, T., and Sakmann, B. (2004). Single spine Ca²⁺ signals evoked by coincident EPSPs and backpropagating action potentials in spiny stellate cells of layer 4 in the juvenile rat somatosensory barrel cortex. *J. Neurosci.* *24*, 1689–1699.
- Nevian, T., Larkum, M.E., Polsky, A., and Schiller, J. (2007). Properties of basal dendrites of layer 5 pyramidal neurons: a direct patch-clamp recording study. *Nat. Neurosci.* *10*, 206–214.
- Pettit, D.L., Wang, S.S.H., Gee, K.R., and Augustine, G.J. (1997). Chemical two-photon uncaging: a novel approach to mapping glutamate receptors. *Neuron* *19*, 465–471.
- Poirazi, P., and Mel, B.W. (2001). Impact of active dendrites and structural plasticity on the memory capacity of neural tissue. *Neuron* *29*, 779–796.
- Poirazi, P., Brannon, T., and Mel, B.W. (2003a). Pyramidal neuron as two-layer neural network. *Neuron* *37*, 989–999.
- Poirazi, P., Brannon, T., and Mel, B.W. (2003b). Arithmetic of subthreshold synaptic summation in a model CA1 pyramidal cell. *Neuron* *37*, 977–987.
- Poleg-Polsky, A., Ding, H., and Diamond, J.S. (2018). Functional compartmentalization within starburst amacrine cell dendrites in the retina. *Cell Rep.* *22*, 2898–2908.
- Polsky, A., Mel, B., and Schiller, J. (2009). Encoding and decoding bursts by NMDA spikes in basal dendrites of layer 5 pyramidal neurons. *J. Neurosci.* *29*, 11891–11903.
- Rhodes, P. (2006). The properties and implications of NMDA spikes in neocortical pyramidal cells. *J. Neurosci.* *26*, 6704–6715.
- Rotter, S., and Diesmann, M. (1999). Exact digital simulation of time-invariant linear systems with applications to neuronal modeling. *Biol. Cybern.* *81*, 381–402.
- Rudolph, M., and Destexhe, A. (2003). A fast-conducting, stochastic integrative mode for neocortical neurons in vivo. *J. Neurosci.* *23*, 2466–2476.
- Russell, S.J., and Norvig, P. (2003). *Artificial Intelligence: A Modern Approach* (Pearson Education).
- Sacramento, J., Costa, R.P., Bengio, Y., and Senn, W. (2017). Dendritic error backpropagation in deep cortical microcircuits. *arXiv*, arXiv:1801.00062v1.
- Schiess, M., Urbanczik, R., and Senn, W. (2016). Somato-dendritic synaptic plasticity and error-backpropagation in active dendrites. *PLoS Comput. Biol.* *12*, e1004638.
- Segev, I., and London, M. (2000). Untangling dendrites with quantitative models. *Science* *290*, 744–750.
- Silver, R.A. (2010). Neuronal arithmetic. *Nat. Rev. Neurosci.* *11*, 474–489.
- Simon, S.M., and Llinás, R.R. (1985). Compartmentalization of the submembrane calcium activity during calcium influx and its significance in transmitter release. *Biophys. J.* *48*, 485–498.
- Takahashi, N., Oertner, T.G., Hegemann, P., and Larkum, M.E. (2016). Active cortical dendrites modulate perception. *Science* *354*, 1587–1590.
- Torben-Nielsen, B., and Stiefel, K.M. (2010). An inverse approach for elucidating dendritic function. *Front. Comput. Neurosci.* *4*, 128.
- Ujfalussy, B.B., Makara, J.K., Lengyel, M., and Branco, T. (2018). Global and multiplexed dendritic computations under in vivo-like conditions. *Neuron* *100*, 579–592.e5.
- Urbanczik, R., and Senn, W. (2014). Learning by the dendritic prediction of somatic spiking. *Neuron* *81*, 521–528.
- Vetter, P., Roth, A., and Häusser, M. (2001). Propagation of action potentials in dendrites depends on dendritic morphology. *J. Neurophysiol.* *85*, 926–937.
- Wang, Y., Gupta, A., Toledo-Rodriguez, M., Wu, C.Z., and Markram, H. (2002). Anatomical, physiological, molecular and circuit properties of nest basket cells in the developing somatosensory cortex. *Cereb. Cortex* *12*, 395–410.

- Waters, J., and Helmchen, F. (2004). Boosting of action potential backpropagation by neocortical network activity in vivo. *J. Neurosci.* *24*, 11127–11136.
- Weber, J.P., Andrásfalvy, B.K., Polito, M., Magó, Á., Ujfalussy, B.B., and Markara, J.K. (2016). Location-dependent synaptic plasticity rules by dendritic spine cooperativity. *Nat. Commun.* *7*, 11380.
- Wei, D.-S., Mei, Y.-A., Bagal, A., Kao, J.P.Y., Thompson, S.M., and Tang, C.-M. (2001). Compartmentalized and binary behavior of terminal dendrites in hippocampal pyramidal neurons. *Science* *293*, 2272–2275.
- Wilson, C.J., and Kawaguchi, Y. (1996). The origins of two-state spontaneous membrane potential fluctuations of neostriatal spiny neurons. *J. Neurosci.* *16*, 2397–2410.
- Wybo, W.A.M., Stiefel, K.M., and Torben-Nielsen, B. (2013). The Green's function formalism as a bridge between single- and multi-compartmental modeling. *Biol. Cybern.* *107*, 685–694.
- Wybo, W.A.M., Boccalini, D., Torben-Nielsen, B., and Gewaltig, M.-O. (2015). A sparse reformulation of the Green's function formalism allows efficient simulations of morphological neuron models. *Neural Comput.* *27*, 2587–2622.
- Yuste, R., and Denk, W. (1995). Dendritic spines as basic functional units of neuronal integration. *Nature* *375*, 682–684.
- Zador, A.M., Agmon-Snir, H., and Segev, I. (1995). The morphoelectrotonic transform: a graphical approach to dendritic function. *J. Neurosci.* *15*, 1669–1682.

STAR★METHODS

KEY RESOURCES TABLE

Reagent or Resource	Source	Identifier
Deposited Data		
Hippocampal granule cell	Carim-Todd et al. (2009)	NeuroMorpho.Org ID: NMO_07645
Cortical stellate cell	Wang et al. (2002)	NeuroMorpho.Org ID: NMO_00274
Cortical L5 pyramidal cell	Hay et al. (2011)	ModelDB entry: 139653
Other cortical cells	Markram et al. (2015)	https://bbp.epfl.ch/nmc-portal/welcome
Plasticity model	Bono and Clopath (2017)	https://doi.org/10.1038/s41467-017-00740-z
Other		
Basal dendrites neocortical L5 pyramidal cells	Nevian et al. (2007)	N/A

CONTACT FOR REAGENT AND RESOURCE SHARING

Further information and requests for resources and reagent should be directed to and will be fulfilled by the Lead Contact, Benjamin Torben-Nielsen (btorbennielsen@gmail.com).

METHOD DETAILS

Biophysical modeling

Morphologies

Three exemplar morphologies were used for the analysis: a cortical stellate cell ([Wang et al., 2002](#)) (Figure 2A), a hippocampal granule cell ([Carim-Todd et al., 2009](#)) (Figure 2B) and a cortical pyramidal cell ([Hay et al., 2011](#)) (Figure 2C). These morphologies were retrieved from the [NeuroMorpho.org](#) repository ([Ascoli, 2006](#)), except the pyramidal cell, which was retrieved from the ModelDB repository ([Hines et al., 2004](#)). Cell morphologies used in our wider cortical analysis were retrieved from the Blue Brain Project database ([Markram et al., 2015](#)).

Physiological parameters

Physiological parameters for the morphologies were set according to [Major et al. \(2008\)](#): the equilibrium potential was -75 mV, the membrane conductance $100 \mu\text{S}/\text{cm}^2$, the capacitance $0.8 \mu\text{F}/\text{cm}^2$ and the intracellular resistance $100 \Omega \cdot \text{cm}$.

To generate somatic APs, we used the fast inactivating Na^+ current (g_{Nat}) and the fast, non-inactivating K^+ current ($g_{\text{Kv3.1}}$) previously employed in cortical models ([Hay et al., 2011](#)). Channel densities were: $\bar{g}_{\text{Nat}} = 1.71 \text{ S}/\text{cm}^2$ and $\bar{g}_{\text{Kv3.1}} = 0.766 \text{ S}/\text{cm}^2$. The leak current was then fitted to yield a membrane timescale of 10 ms and an equilibrium potential of -75 mV.

AMPA and GABA synaptic input currents were modeled as the product of a conductance profile, given by a double exponential shape ([Rotter and Diesmann, 1999](#)), with a driving force ([Jack et al., 1975](#)):

$$I_{\text{syn}}(t) = g(t) \cdot (E_r - V(t)). \quad (\text{Equation 7})$$

For AMPA synapses, we used rise resp. decay times $\tau_r = 0.2$ ms, $\tau_d = 3$ ms for the conductance window and a reversal potential $E_r = 0$ mV, while for GABA synapses we used $\tau_r = 0.2$ ms, $\tau_d = 10$ ms and $E_r = -80$ mV. For N-methyl-D-aspartate (NMDA) channels ([Jahr and Stevens, 1990a](#); [MacDonald and Wojtowicz, 1982](#)), the synaptic current had the form

$$I_{\text{syn}}(t) = g(t) \cdot (E_r - V(t)) \sigma(V(t)) \quad (\text{Equation 8})$$

and the rise resp. decay time were $\tau_r = 0.2$ ms, $\tau_d = 43$ ms, and $E_r = 0$ mV, while $\sigma(V)$ was the sigmoidal function employed by ([Behabadi and Mel, 2014](#)) to model the channels' magnesium block:

$$\sigma(V) = \frac{1}{1 + 0.3 e^{-0.1 V}}. \quad (\text{Equation 9})$$

We also tested our results with the original gating function by [Jahr and Stevens \(1990b\)](#):

$$\sigma(V) = \frac{1}{1 + \frac{e^{-0.062 V}}{3.57}} \quad (\text{Equation 10})$$

and the voltage dependence of the NMDA conductance in spiny stellate cells ([Lavzin et al., 2012](#)):

$$\sigma(V) = \frac{1}{1 + 0.25 e^{-0.08 V}}. \quad (\text{Equation 11})$$

In the remainder of this work, we will refer to the voltage-dependent factors in the synaptic input current as the ‘synaptic voltage dependence’ (SVD), denoted by $f(V)$. Hence, for AMPA or GABA synapses

$$f(V) = E_r - V \quad (\text{Equation 12})$$

and for NMDA synapses

$$f(V) = (E_r - V)\sigma(V). \quad (\text{Equation 13})$$

Note that when we refer to the conductance of a simple synapse, we mean the maximum value g_{\max} of its conductance window. For a synapse that has AMPA and NMDA components (to which we will simply refer as an NMDA synapse), the conductance is the maximal value of the AMPA conductance window, and the conductance of the NMDA component is determined by multiplying the AMPA conductance value with an NMDA ratio R_{NMDA} , that was set to be either 2 or 3.

Plasticity

In our simulations with plasticity, we use a voltage dependent spike timing dependent plasticity rule ([Bono and Clopath, 2017](#); [Clopath et al., 2010](#)) where the evolution of the weight $w(t)$ of a given synapse depends both on the post-synaptic voltage and the pre-synaptic AP inputs. This leads to a synaptic current of the following form:

$$I_{\text{syn}}(t) = w(t)g(t)f(V(t)). \quad (\text{Equation 14})$$

In all our simulations the initial weight $w(t=0)$ was 1 and, during the simulation, the weight could fluctuate in the interval $[0, 2]$.

Compartmental models

To construct and simulate compartmental models of the cells, we used the NEURON simulator ([Carnevale and Hines, 2004](#)). Compartment sizes were set to be smaller than or equal to the size given by the lambda rule ([Carnevale and Hines, 2004](#)).

Green’s function and the separation of variables

To derive NETs, we rely on the Green’s function (GF) ([Koch, 1998](#); [Wybo et al., 2013, 2015](#)) $Z(x, x', t)$. The GF is a function of three variables: two locations x and x' along the dendritic arborization and a temporal variable t . We compute the GF in an exponential basis:

$$Z(x, x', t) = \sum_{k=0}^{\infty} \phi_k(x)\phi_k(x')e^{-\frac{t}{\tau_k}} \quad (\text{Equation 15})$$

by using the separation of variables (SOV) method ([Major and Evans, 1994](#); [Major et al., 1993](#)). Note that it is a property of the cable equation that the GF is symmetric in the spatial coordinates ([Koch, 1998](#)), so that $Z(x, x', t) = Z(x', x, t)$. Usually, a fixed set of discrete locations relevant for the problem at hand is chosen on the neuron. Hence, the GF only needs to be evaluated at these locations, and a discrete set of temporal *kernels* is obtained. A member of this set will be denoted as $Z_{x, x'}(t)$, to highlight the difference between the now discrete indices x and x' and the continuous variable t .

To compute the output voltage $V_x(t)$ at location x for a given input current $I_{x'}(t)$ at location x' , one needs to compute the convolution of the GF evaluated at x and x' with this input current ([Koch, 1998](#)):

$$V_x(t) = \int_0^{\infty} ds Z_{x, x'}(s) I_{x'}(t - s) \quad (\text{Equation 16})$$

for which we will use the shorthand

$$V_x(t) = Z_{x, x'}(t) * I_{x'}(t). \quad (\text{Equation 17})$$

Since $Z_{x, x'}(t)$ converts current into voltage, we will refer to it as an ‘impedance kernel.’ The total surface under the impedance kernel is the steady state impedance:

$$Z_{x, x'} = \int_0^{\infty} dt Z_{x, x'}(t). \quad (\text{Equation 18})$$

In the rest of the text, it will be understood that $Z_{x,x'}$ without temporal coordinate refers to the steady state impedance – which we will simply call ‘the impedance’ for brevity – while $Z_{x,x'}(t)$ is the temporal impedance kernel. To unclutter the notations, we will not make this distinction for other variables; the temporal dependence will be omitted by default. Following this convention, Equation (17) will be written as $V_x = Z_{x,x'}(t) * I_{x'}$, where it is implied that both $I_{x'}$ and V_x are time dependent quantities since $Z_{x,x'}(t)$ is the temporal impedance kernel. Conversely, writing $V_x = Z_{x,x'} I_{x'}$ means that $Z_{x,x'}$ is the steady state impedance value, and thus $I_{x'}$ and V_x will be steady state values too. Note that currents in this text will be expressed in nano ampere (nA) and voltages in milli volt (mV). Consequently, impedances will be in mega ohm (MΩ).

Synaptic activation

The eventual steady state voltage V_x obtained after activating a synaptic conductance at location x depends for a large part on the input impedance $Z_{x,x}$. Following (17), it can be obtained as a solution of the equation

$$V_x = Z_{x,x} g f(V_x). \quad (\text{Equation 19})$$

This solution D is thus a function of the product of impedance and conductance:

$$V_x = D(Z_{x,x} g). \quad (\text{Equation 20})$$

We refer to this product as the synaptic activation $A_x = Z_{x,x} g$ and note that it is a dimensionless quantity. Consequently, it is a convenient quantity that does not depend on local morphological constraints to determine whether an input will be strong enough to reach a certain voltage threshold, for instance to elicit an NMDA spike or to potentiate a synapse.

Neural Evaluation tree

Mathematical formulation

In the NET framework, the voltage at a node can be expressed as:

$$\bar{V}_N(t) = \bar{Z}_N(t) * \sum_{r \in \mathcal{R}_N} \sum_{s \in \mathcal{S}_r} g_s(t) f_s \left(\sum_{M \in \mathcal{N}_r} \bar{V}_M(t) \right), \quad (\text{Equation 21})$$

where \mathcal{R}_N is the set of all input regions a node N integrates, \mathcal{S}_r the set of all synapse types at region r (with g_s their conductance and $f_s(\cdot)$ their SVD) and \mathcal{N}_r the set of all nodes that integrate region r . $\bar{Z}_N(t)$ resp. $\bar{V}_N(t)$ denote the impedance kernel resp. voltage at node N . Note that at the NET leafs, each node integrates inputs from only one region. Note furthermore that the matrix associated with this system can be inverted in $O(n)$ steps (with n the number of nodes), so that efficient NET simulations can be designed (see Methods S1).

Derivation

To derive the NET, we order all locations along the dendritic arborization in a depth-first manner (Russell and Norvig, 2003) (Figures S1A–S1C), so that the impedance matrix (Cuntz et al., 2010) has a highly organized structure (Figures 1C and 1D). Generally an even blue surface covers most of the matrix, representing the transfer impedances between the main dendritic branches. There are also smaller square regions of light blue or green closer to the diagonal, representing sibling branches that are electrically closer to each other than to different main branches. Finally, the small squares along the diagonal colored yellow and red are the thin dendritic tips with high input impedances. Consequently, dendritic tips that lie within the same light blue or green square are closer together electronically than tips within different squares, as the transfer impedances connecting them are much higher. A NET tree graph structure hence imposes itself naturally: the dendritic tips constitute the leafs of the tree, their parent node combines multiple adjacent tips and the root node in turn binds all these nodes together. To derive the NET tree graph, we define an impedance step ΔZ and execute the following recursively:

1. Let k denote the step number. We assume that a value $Z_{\min,k}$ is at our disposition. In the first step this value is 0, in later steps it is given by the previous steps. A value $Z_{\max,k}$ is also determined, in the first step as the somatic input impedance (Z_{00} with our depth-first ordering of the impedance matrix) and in later steps by $Z_{\max,k} = Z_{\min,k} + \Delta Z$.
2. The kernel of the current node is constructed as the average of all impedance kernels associated with points in the impedance matrix for which $Z_{\min,k} \leq Z_{ij} < Z_{\max,k}$ (colored blue in Figure 1E). This approach is justified, as impedance kernels of similar magnitude have similar timescales (Figure 1B). Then, the kernels of all nodes on the path from the current node’s parent node to the root node are subtracted from this average kernel.
3. The current node’s child nodes are determined from the input impedance, located on the diagonal of the impedance matrix. Due to the depth-first ordering, new nodes can be identified as uninterrupted intervals on this diagonal where $Z_{ii} > Z_{\max,k}$ (Figure 1F). For each of these intervals, a new child node is constructed by repeating step 1 with the impedance matrix restricted to the interval (indicated in Figure 1G by the red squares) and with $Z_{\min,k+1} = Z_{\max,k}$. When $Z_{\max,k} > \max_i Z_{ii}$, the algorithm does not continue and the current node remains a leaf node.

Generally, one aims to study a subset of “regions of interest” on the dendritic tree. In such cases, the original NET can be pruned so that a strongly reduced NET is obtained. The pruning consist of two operations: First, nodes that do not integrate regions of interest are removed. Second, nodes that integrate the same subset of the regions of interest are combined into a single node, whose

impedance kernel is the sum of the impedance kernels of the original nodes. This reduced NET is then the minimal structure that faithfully captures the interactions between the regions of interest. As an example, if we would reduce the set of inputs {1, 2, 3, 4, 5} in Figure 1A to {1, 2, 4, 5}, the pink and green nodes both integrate the identical subset {1, 2}. Hence, in the reduced NET, these nodes can be combined into a single node by the aforementioned procedure.

The NET framework can thus be understood as a discretization in “impedance,” instead of in space (as is the case for classical biophysical models). The average error of the NET approximation depends on ΔZ – in analogy to the average error in classical biophysical models, which depends on Δx . Nevertheless, because of the inherent approximations present in the NET framework, the average error does not go to zero but reaches a minimum value for $\Delta Z \lesssim 20 \text{ M}\Omega$ (Figure S4B). 20 M Ω is thus a good choice for ΔZ .

In order to simulate in the NET framework, we have derived an efficient simulation algorithm for Equation (21) (see Methods S1 for details)

Distal and proximal regions

The aforementioned algorithm successfully constructs NETs of dendritic arborization where the variations in transfer impedance between branches are small compared to their average values (Figures S4C–S4E). If these variations are large, as is the case in pyramidal cells (Figure S4E), interactions between proximal and distal dendritic domains are overestimated. In pyramidal cells, distal domains are only connected to the soma by one or a few large dendritic branches. Hence, there are many points of low soma to dendrite impedance Z_{0x} , many of high Z_{0x} , and relatively few of intermediate Z_{0x} . By consequence, the histogram of all dendrite to soma transfer impedances has two main modes, whose boundary (Delon et al., 2007) indicates the domains. Any region with Z_{0x} above this boundary will belong to the proximal domain (node c_0 in Figure S4E), whereas connected regions with Z_{0x} below this boundary will constitute distal domains (colored red in Figure S4E, node c_1). Algorithmically, we determine the kernel of the root node as the average of all transfer impedance kernels between proximal and distal branches. Then, we start the recursive procedure as before, but with the impedance matrices restricted to the different domains c_i .

Predicting spikes: linear terms

The effective NET transfer impedance between dendrite and soma is either constant or can take on a proximal and a distal value. Spike prediction is refined further by defining linear terms that capture the precise transfer impedance between input regions and soma. These kernels only contribute to the voltage at the soma, and thus have no influence on the intra-dendritic synaptic interactions. Mathematically, their contribution to the somatic voltage can be written as:

$$V_{\text{lin}} = \sum_r \bar{Z}_r(t) * \left[\sum_{s \in S_r} g_s f \left(\sum_{M \in \mathcal{N}_r} \bar{V}_M \right) \right]. \quad (\text{Equation 22})$$

Independence and compartmentalization

Independence

The leaves of the NET only receive inputs from a single region. Nevertheless, they are not per se independent from the other synapses, since the SVD in their input current still depends on all nodal voltages on the path to the root:

$$\bar{i}_{g,L}(\bar{\mathbf{V}}) = \sum_{s \in S_L} g_s f_s \left(\bar{V}_L + \sum_{N \in \mathcal{N}_L\{L\}} \bar{V}_N \right). \quad (\text{Equation 23})$$

This current will become truly independent from all other synapses if

$$\delta \bar{V}_L > C \sum_{N \in \mathcal{N}_L\{L\}} \delta \bar{V}_N, \quad (\text{Equation 24})$$

with C a (large) number that has to be determined empirically and $\delta \bar{V}$ denoting the short term fluctuations of \bar{V} around a long term average $\langle \bar{V} \rangle$. Here, short term means the time-scale on which neurons convert electrical inputs to output. As NMDA synapses have a decay time constant of 43 ms, this averaging time-scale should be at least somewhat larger than the NMDA time constant (we chose ~ 200 ms). Then (23) can be approximated as follows:

$$\bar{i}_{g_s,L}(\bar{V}_L) = \sum_{s \in S_L} g_s f_s \left(\bar{V}_L + \left\langle \sum_{N \in \mathcal{N}_L\{L\}} \bar{V}_N \right\rangle \right). \quad (\text{Equation 25})$$

The long-term average in this equation is only influenced very little by the instantaneous values of the synaptic conductances and can hence be seen as a constant, i.e., a fixed parameter in the equation:

$$\bar{V}_L = \bar{Z}_L(t) * \left[\sum_{s \in S_L} g_s f_s \left(\bar{V}_L + \left\langle \sum_{N \in \mathcal{N}_L\{L\}} \bar{V}_N \right\rangle \right) \right]. \quad (\text{Equation 26})$$

Consequently, the solution for \bar{V}_L will not depend on the instantaneous values of the synaptic conductances at other locations.

Estimating independence

Whether condition (24) holds depends on the structure of the NET as well as the relative size of the synaptic inputs. We assume that synaptic conductances in physiological regimes are of similar magnitude. In this case, condition (24) becomes a condition on the impedances:

$$\bar{Z}_L > C \sum_{N \in \mathcal{N}_L(L)} \bar{Z}_N |\mathcal{R}_N|, \quad (\text{Equation 27})$$

where $|\mathcal{R}_N|$ denotes the number of regions node N integrates. When we are interested in determining whether a pair of regions r_i (integrated by the leafs L_i , $i = 1, 2$) can act independently, we can consider a reduced tree with two leafs, obtained by pruning all nodes associated with other regions. The new tree then has leaf impedances $\bar{Z}_i = \sum_{N \in \mathcal{N}_{L_i} / (\mathcal{N}_{L_1} \cap \mathcal{N}_{L_2})} \bar{Z}_N$ (i.e., a sum over impedances of nodes that integrate one region but not the other) and a root impedance $\bar{Z}_R = \sum_{N \in (\mathcal{N}_{L_1} \cap \mathcal{N}_{L_2})} \bar{Z}_N$ (i.e., a sum over impedances of nodes that integrate both regions). Then, regions r_i are independent if:

$$\bar{Z}_{L_i} > 2 C \bar{Z}_R. \quad (\text{Equation 28})$$

For mutual independence between r_1 and r_2 , this equation has to hold for both $i = 1$ and $i = 2$. To summarize these two conditions in a single expression, we defined the ‘impedance-based independence index’ (I_Z):

$$I_Z = \frac{\bar{Z}_1 + \bar{Z}_2}{2 \bar{Z}_R}. \quad (\text{Equation 29})$$

Then, if (28) holds for both regions, the following condition also holds:

$$I_Z > 2 C. \quad (\text{Equation 30})$$

Note that this is a necessary, but not a sufficient condition for mutual independence. However, as shown throughout the main manuscript, when asymmetry is not too high I_Z is, despite its simplicity, a surprisingly accurate measure.

Compartmentalization

Previously we discussed the conditions under which a single input site can be considered independent from the rest of the input regions. Nevertheless, when inputs are distributed in an almost continuous fashion along the dendritic arborization, such sites may not exist. It can be expected, however, that the structure of the dendritic tree favors a grouping of inputs, such that inputs belonging to different groups are all mutually independent but inputs belonging to the same group are not. A grouping of this type for homogeneously distributed inputs along the dendritic arborization, and where inputs belonging to different groups have an I_Z above a certain threshold, will be called a compartmentalization of that dendritic tree for that given I_Z . Note that in such a compartmentalization, *not all input sites can belong to a group*, as there will have to be at least some space between compartments.

How can such a compartmentalization be found? First, we remark that there is no unique answer to this question. Consider a forked dendritic tip. It may happen that inputs within each sister branch are independent from the rest of the dendritic tree, but the branches are not independent from each other. Furthermore, because of a steep impedance gradient within the branch, inputs at the bifurcation point may not be independent from the rest of the tree. Because of the first constraint, both tips can not form separate compartments, whereas because of the second constraint, they can not be grouped into a single compartment either. Hence only one branch can be chosen, and either choice forms a valid compartmentalization.

We implemented an algorithm that proposes, using the NET and given an I_Z , a compartmentalization that maximizes the number of compartments. Intuitively, the algorithm works by removing one leaf branch of a pair when the pair does not form separate compartments. By continuing this until every pair of leaf branches forms separate compartments, a maximal compartmentalization has been found. We note that if a node N in the NET tree forms a valid compartment, all nodes in the subtree of N are part of the same compartment, since their I_Z to other compartments will be higher than the I_Z of N . Hence, our algorithm will simply return a set of nodes, where it is understood that a compartment associated with a node from this set is its whole subtree. Our algorithm proceeds in three steps:

1. We determine a ‘tentative’ compartmentalization. For each node N in the NET tree, we examine the bifurcation nodes B on the path \mathcal{N}_N from N to the root. We check whether the following condition holds

$$I_Z < \frac{\sum_{K \in \mathcal{N}_N \setminus \mathcal{N}_B} \bar{Z}_K}{\sum_{K \in \mathcal{N}_B} \bar{Z}_K}, \quad (\text{Equation 31})$$

- with \mathcal{N}_b the path from B to the root. If this condition is true for two nodes N and M that have B on their respective paths to the root, and where $(\mathcal{N}_N/\mathcal{N}_B) \cap (\mathcal{N}_M/\mathcal{N}_B) = \emptyset$, these nodes will be separated by at least the required I_Z . Hence, we say that N is a tentative compartment with respect to B .
- In a second step, we remove all leaves from the tree that could not possibly be separate compartments. To do so, we look at the highest order bifurcation B and its child leaves. Then, if at least two child leaves are tentative compartments with respect to B , the other leaves are removed. Otherwise, all child leaves but the one with largest impedance are removed. Note that in the latter case, B is not a bifurcation anymore and consequently will not induce tentative compartments. We continue to cycle through the bifurcation nodes of highest order until no more nodes can be removed.
- In a final step we assign the compartments. As we are now sure that every leaf is part of a separate compartment, we start at the leaf, find the nearest bifurcation node in the NET tree, and then recursively find the lowest order node that is still a tentative compartment of B . This node will be a compartment node in the final compartmentalization.

Extracting I_Z from patch-clamp data

Extrapolating from two-electrode recordings

Although there was only data available from two-electrode patch clamp setups with one dendritic and one somatic electrode, it is still possible to extrapolate what the value of I_Z would be between two dendritic locations, if the second location (D_2) would be on a branch with similar electrical properties and at a similar distance from the soma as the first location (D_1). From the dendritic current injection, we can calculate the input impedance Z_{D_1,D_1} and the dendrite-to-soma transfer impedance Z_{SD_1} by fitting a regression line to the IV-curve. Conversely, from the somatic current injection, we can calculate the somatic input impedance Z_{SS} as well as the soma-to-dendrite transfer impedance $Z_{D_1,S}$ in a similar manner. We then assume that $Z_{D_2,D_2} \approx Z_{D_1,D_1}$, $Z_{SD_2} \approx Z_{SD_1}$ and $Z_{D_2,S} \approx Z_{D_1,S}$. I_Z between these two sites is given by:

$$I_Z(D_1, D_2) = \frac{\bar{Z}_{D_1} + \bar{Z}_{D_2}}{2\bar{Z}_R}, \quad (\text{Equation 32})$$

with $\bar{Z}_{D_1} = Z_{D_1,D_1} - \bar{Z}_R$, $\bar{Z}_{D_2} = Z_{D_2,D_2} - \bar{Z}_R$ and $Z_R = Z_{D_1,D_2}$ the transfer impedance between both dendritic sites. The latter impedance can be estimated from the transitivity property (Koch, 1998):

$$Z_{D_1,D_2} = \frac{Z_{D_1,S} Z_{SD_2}}{Z_{SS}} \approx \frac{Z_{D_1,S} Z_{SD_1}}{Z_{SS}}. \quad (\text{Equation 33})$$

Estimating the dendritic access resistance

Full compensation of whole-cell current clamp recordings are difficult due to the positive feedback of the electronic compensation circuitry that can lead to ringing and disruption of the giga seal (Brette and Destexhe, 2012). This is particularly the case when high resistance pipettes have to be used as in the case of recordings from the basal dendrites of pyramidal neurons. The compensation of capacitance and access resistance during the experiment was performed following standard procedures aiming optimal compensation, while avoiding overcompensation and ringing. Additional offline compensation was achieved by fitting the initial change in membrane voltage at the dendritic and somatic recording site with a double exponential function (Anderson et al., 2000; De Sa and MacKay, 2001):

$$f(t) = c_1 e^{-\frac{t}{\tau_1}} + c_2 e^{-\frac{t}{\tau_2}} \quad (\text{Equation 34})$$

to the voltage transient after stimulus onset. To do so, we minimized a weighted sum of squares error

$$E(c_1, \tau_1, c_2, \tau_2) = \sum_t (w(t)(f(t) - V(t)))^2, \quad (\text{Equation 35})$$

where the weights were given by $w(t) = 1/(1 + t/\tau)$ (with $\tau = 1$ ms), a function chosen to prioritize accuracy at small t values (Figures S5A and S5B). The resulting fit $f(t)$ contained one fast and one slow time-scale (let us index the fast time-scale with 1), and we equated the superfluous voltage drop due to the access resistance to the prefactor of the fastest exponential:

$$\Delta V_{\text{access}} = c_1. \quad (\text{Equation 36})$$

It can be seen that this analysis yielded a co-linear set of values for the different injected current amplitudes in each experiment (Figure 5C). An estimate of the access resistance was then obtained from the slope of the regression line between ΔV_{access} and the amplitude of the injected current step.

To estimate the variability of our approximations of the access resistance, we also performed the same procedure at the soma, where the access resistance for each experiment could be determined from the standard bridge-balance procedure. We then compared fitted resistances with the values yielded by bridge balance (Figure 5D) and found good agreement within the limits of experimental variability. The distribution of these values then provided an estimate of the variability in our fit (Figure S5D), which allowed us to compute the uncertainty of our access resistance fit and yielded the error flags (Figure S5E).

Simulation-specific parameters

Parameters Figure 1.

We evaluated the impedance matrix in panel B at 10 μm intervals. In the simulation depicted in panels J and K, the synapses contained only an AMPA component with $g_{\text{max}} = 10$ nS and no active channels were inserted in the soma.

Parameters Figure 2.

100 NMDA ($g_{\text{max}} = 4$ nS and $R_{\text{NMDA}} = 3$) and 100 GABA ($g_{\text{max}} = 2$ nS) synapses were inserted on the morphology and activated with Poisson spike trains of 1 Hz.

Parameters Figure 3.

The synapse at region 1 was an NMDA synapse with $g_{\text{max}} = 1$ nS and $R_{\text{NMDA}} = 3$. The synapse received 5 input spikes in a 2.5 ms interval in order to trigger an NMDA spike

Parameters Figure 4.

For the simulations in panels C-D, NMDA synapses ($R_{\text{NMDA}} = 3$) were used. Their g_{max} and incoming Poisson rate were optimized to utilize the full range of the NMDA non-linearity. For the simulations in panel E, NMDA ($g_{\text{max}} = 2$ nS and $R_{\text{NMDA}} = 2$) and GABA ($g_{\text{max}} = 1$ nS) synapses were used and their rates were also optimized to utilize the full range of the NMDA non-linearity.

Parameters Figure 6.

For the simulations in panel C, the main synapses contained only an AMPA component with $g_{\text{max}} = 5$ nS. To simulate the high-conductance state, 200 AMPA and 200 GABA synapses ($g_{\text{max}} = 0.5$ nS) were distributed evenly across the neuron. Each AMPA synapse was stimulated with a Poisson spike train of 5 Hz. The rate of stimulation for the GABA synapses was tuned to achieve a balanced input. To recompute the tree structures for panels B and D, the time-averaged conductances of all background synapses were inserted in the morphology as static shunts.

The inhibitory synapse in panels E-H had $g_{\text{max}} = 2.3$ nS and was activated at a steady rate of 200 Hz, so that its total time-averaged conductance was around 5 nS. For the simulations in panel H, we inserted NMDA synapses ($R_{\text{NMDA}} = 3$) in both branches and stimulated them with a rate of 200 Hz. Note that these inputs could come from multiple presynaptic cells. Due to the linearity of the conductance dynamics however all spikes can be taken to add to the same conductance and can hence be modeled as a single synapse. The maximal conductance g_{max} of the NMDA synapse was optimized to obtain an average depolarization of -40 ± 2.5 mV in each branch, a target value which yields parameters that allow exploitation of the full range of the NMDA non-linearity.

Parameters Figure 7.

In both simulations with and without shunting inhibition, noise was implemented at all three locations using AMPA ($g_{\text{max}} = 0.1$ nS) and GABA ($g_{\text{max}} = 0.2$ nS) synapses. Both were stimulated with Poisson spike trains of resp. 33 Hz and 83.1 Hz (tuned to achieve balance). The shunting inhibition in the parent branch was implemented by a GABA synapse ($g_{\text{max}} = 2$ nS) receiving a Poisson train with a rate of 277 Hz (tuned to reach a time-averaged conductance of 12 nS) during the 100 ms learning intervals. Note that this single conductance could again represent multiple synapses.

Stimulus-specific innervation patterns were: $S(\uparrow)$ to $B(\uparrow)$: 5 synapses, $S(\uparrow)$ to $B(\downarrow)$: 2 synapses, $S(\downarrow)$ to $B(\uparrow)$: 2 synapses and $S(\downarrow)$ to $B(\downarrow)$: 5 synapses. These synapses were all NMDA synapses ($g_{\text{max}} = 0.6$ nS, $R_{\text{NMDA}} = 2$) that were activated in the learning intervals with Poisson trains at a rate of 33.3 Hz without the shunting inhibition and 39.8 Hz with the shunting inhibition (to compensate for the loss in input impedance in both branches).

Parameters Figure S1.

For the simulation in panels D-F, 10 clusters of 10 excitatory ($g_{\text{max}} = 4$ nS and $R_{\text{NMDA}} = 3$) and 10 inhibitory ($g_{\text{max}} = 2$ nS) synapses were inserted at random, and within each cluster excitatory and inhibitory synapses were evenly spaced at 4 μm intervals. Synapses were activated with Poisson spike trains of 3 Hz.

Parameters Figure S2.

In panel D, synapse 1 was a non-plastic NMDA synapse ($g_{\text{max}} = 1$ nS, $R_{\text{NMDA}} = 3$) and synapse 2 a plastic synapse with the same parameters. When on, synapse 1 received a tonic spike train with a rate of 113 Hz (to yield a time-averaged activation $A_1 \approx 15$). Synapse 2 received rates ranging from 0 to 113 Hz, corresponding to the data points at different activations in the figure in the figure. For the simulations in panel H, we inserted NMDA synapses ($R_{\text{NMDA}} = 3$) in both branches and stimulated them with a rate of 200 Hz. Their maximal conductance g_{max} was optimized to obtain an average depolarization of -40 ± 2.5 mV in each branch.

DATA AND SOFTWARE AVAILABILITY

Code for the derivation of NETs from biophysical neuron models can be found online as part of the NEural Analysis Toolkit (NEAT, <https://github.com/WillemWybo/NEAT>). We provide scripts to reproduce results from this paper (https://github.com/WillemWybo/Electrical_compartmentalization_in_neurons). To run these scripts, NEAT's NEURON extension is also needed (https://github.com/WillemWybo/NEAT_NEURON_extension).

Cell Reports, Volume 26

Supplemental Information

Electrical Compartmentalization in Neurons

Willem A.M. Wybo, Benjamin Torben-Nielsen, Thomas Nevian, and Marc-Oliver Gewaltig

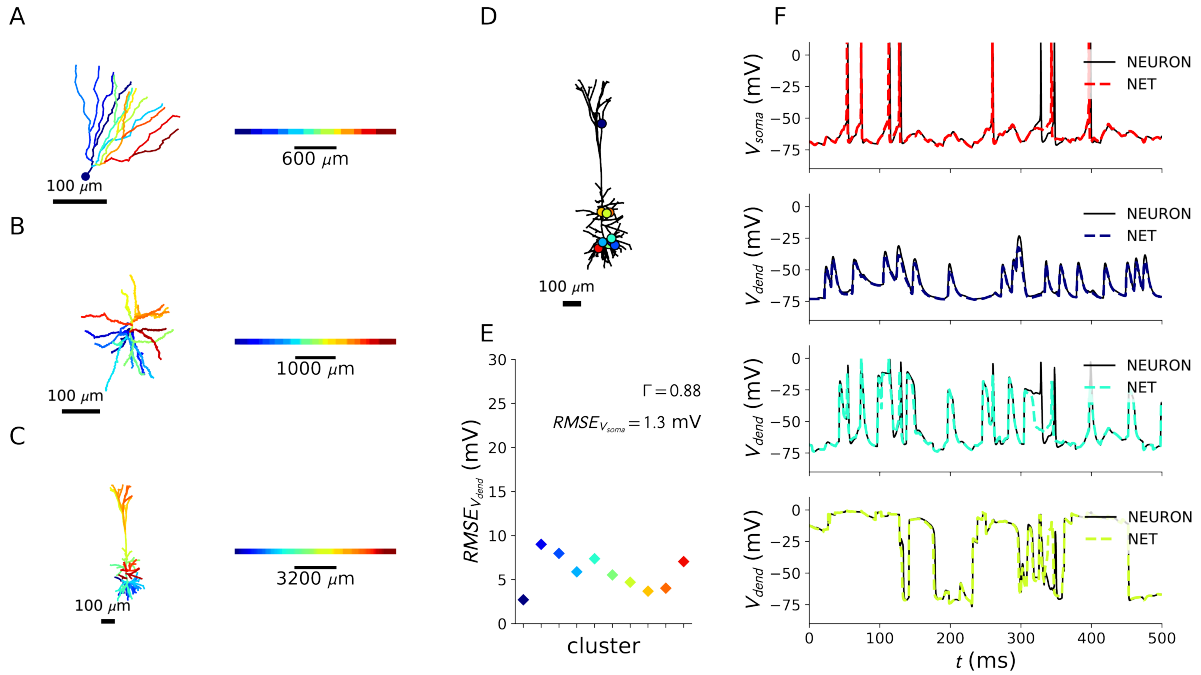


Figure S1. Unravelling of morphologies and validation with clustered input (related to Fig 1, Fig 2). **A-C:** When unravelling the morphologies on a one-dimensional axis, we use a depth-first ordering (Russell and Norvig, 2003): We pick a leaf at random, and first place the regions between the root and that leaf on the x-axis from (with the root on the left and the leaf on the right). We then move back from the leaf to the nearest bifurcation, and plot the regions between that bifurcation and another leaf (in the subtree of the bifurcation) on the x-axis (again, bifurcation on the left and leaf on the right). We then repeat this procedure, until all leaves in the subtree of the bifurcation are passed once. Then, we move back to the next bifurcation closer to the root, and repeat the procedure again, and continue thusly until all leaves have been passed exactly once. We visualize this unravelling for all three morphologies (A: granule cell, B: stellate, C: L5 pyramid) by color coding the branches, and colouring the corresponding regions on x-axis in the same color. **D:** We validated the NET-framework also in case of clustered synapses: to that end, we distributed 10 clusters at random on the morphology (the cluster centroids represented by the coloured circles). Each cluster consisted of 10 excitatory and 10 inhibitory synapses at 4 μm intervals. We then stimulated each synapse with random Poisson inputs at 1 Hz. **E:** The RMSEs at the cluster centroid for each cluster. Spike coincidence Γ and somatic RMSE are also shown. **F:** Comparison of voltage trace between NET (coloured dashed lines) and NEURON model (black lines) for the soma (top) and three of the clusters (line colour corresponds to cluster).

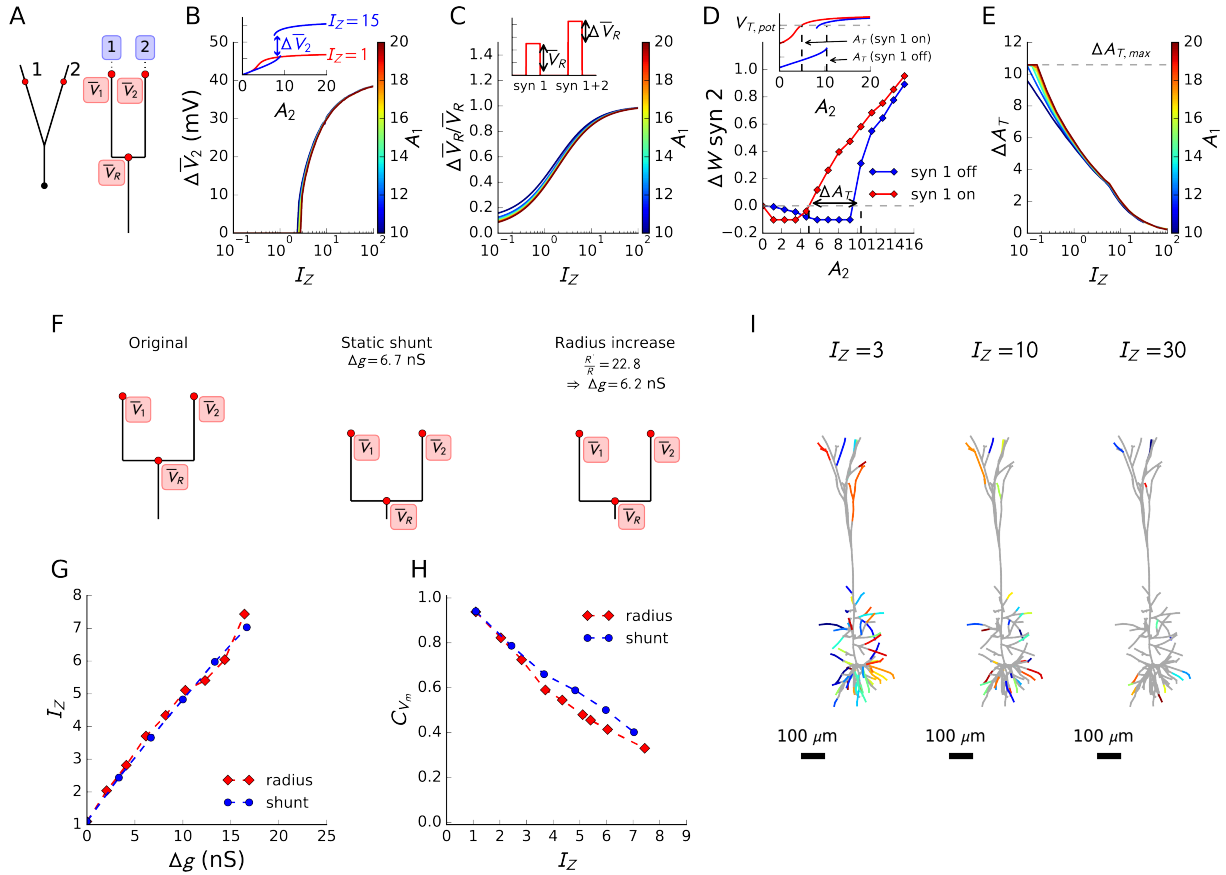


Figure S2. Additional analysis of independent electrical compartments (related to Fig 2, Fig 4). Study of the behaviour of the asymptotic equilibrium points of the NMDA dynamics (A-E) at different levels of synaptic activation (where the activation is defined as the product of input impedance and synaptic conductance, a dimensionless quantity – see methods). **A:** Toy model morphology and associated NET. **B:** Test whether an independent NMDA spike can be generated in branch 2 when there already is an NMDA spike in branch 1. A hallmark of the NMDA-spike is the low and high line of asymptotic equilibrium points as a function of the synaptic activation (inset, blue line – large separation of $I_Z = 15$ between sites, Major et al. (2008)). When the synaptic activation increases sufficiently, the low line of equilibrium points disappears and the voltage jumps to the high line of equilibrium points, generating an NMDA spike. Hence, the amplitude of the jump at site 2 (ΔV_2 in the plot) determines whether an independent NMDA spike can exist at site 2. At $I_Z = 1$ (red line), there is no jump and there can be no independent NMDA spike at site 2. The amplitude of this jump is plotted in the main panel and reaches 80% of its maximum for $I_Z \geq 10$. Colour indicates the amplitude of the activation at synapse 1. The lines for different activations A_1 overlap substantially, indicating that the amplitude of the jump mainly depends on I_Z and not on the precise activation at synapse 1 (as long as A_1 is strong enough to generate an NMDA spike at site 1). **C:** Summation of NMDA events in separate branches depends on I_Z . When branches are independent, NMDA events are expected to sum perfectly in the root voltage \bar{V}_R . In other words, when synapse 1 and 2 are activated above the NMDA spike threshold, the surplus $\Delta \bar{V}_R$ (inset) should be equal to the root voltage when only synapse 1 is activated (here denoted by \bar{V}_R). Their ratio indeed converges to one, independently from the precise activation of the synapses (colour coding), and reaches 80% of its maximum for $I_Z \geq 10$. **D:** Measuring local voltage allows quantification of the influence local branches exert on each other during learning. To do so, we measure the threshold synaptic activation A_T required to potentiate synapse 2, once when synapse 1 is off and once when it is on (inset). For independent synapses, there would be no shift in A_T upon activation of synapse 1 and ΔA_T would be 0. The weight change is shown after 300 ms of tonic stimulation at synapse 2 when synapse 1 was off (blue) and on (red) ($I_Z = 1$). The computed shift in threshold activation ΔA_T required to potentiate synapse 2 is indicated. **E:** The aforementioned shift in threshold activation as a function of I_Z . This shift can not be larger than the threshold for potentiation ($\Delta A_{T,max}$; grey line): When I_Z is very small, the voltage at synapse 2 will always be above the threshold for potentiation when synapse 1 is on. The amplitude of this shift again depends only weakly on the precise level of A_1 (colour coding). For $I_Z \geq 10$, the shift is less than 20% of its maximum value. **F:** We modify I_Z by either adding a static shunt conductance to the parent branch or by increasing its radius. The original NET is shown on the left, the NET for an additional static shunt conductance in the middle and the NET for an increased radius on the right. Note that modifying I_Z by increasing the radius is not realistic in this case: to obtain a sizeable increase in I_Z , the radius had to be multiplied by an unrealistically high factor. **G:** The increase in I_Z by the aforementioned manipulations is determined by the increase in conductance in the parent branch. **H:** The voltage correlation for both ways of increasing I_Z . The inputs were tuned to use the full range of the NMDA non-linearity. **I:** Analysis for the pyramidal cell of the change in compartmentalization when the threshold I_Z between compartments is altered.

	M-type	L5_TTPC1 (2)	L5_TTPC2 (4)	L4_SS (4)	L23_NBC (5)	L23_BTC (3)
Morphometric	Example morphology					
	No. terminals	103.0±16.0	109.8±20.0	28.5±8.8	29.8±4.2	33.3±10.1
	No. main branches	8.5±0.5	8.2±0.8	5.5±0.5	7.6±1.6	4.7±1.2
Electrical	Total length (μm)	16045.7±1634.5	12391.0±2967.9	4020.3±815.4	3590.1±639.0	3692.5±813.0
	Z_{soma} (M Ω)	31.1±3.2	39.0±10.4	109.4±12.1	143.4±13.4	144.0±9.9
	Max Z_{in} (M Ω)	1871.3±570.3	1339.5±511.3	822.6±176.7	1229.1±174.8	2111.0±329.3
NET	Min Z_{trans} (M Ω)	4.5±0.4	7.7±4.8	65.2±17.3	99.6±22.5	84.2±24.6
	No. compartments ($I_Z=1$)	79.5±6.5	65.0±15.2	20.0±3.5	22.6±4.4	22.7±5.7
	No. compartments ($I_Z=3$)	59.0±7.0	44.5±10.3	12.2±4.9	12.6±4.8	11.7±2.6
	No. compartments ($I_Z=10$)	31.0±4.0	24.8±5.0	2.5±4.3	1.4±1.9	4.0±3.6
	No. compartments ($I_Z=30$)	7.0±1.0	9.0±6.4	0.0±0.0	0.0±0.0	0.0±0.0
	% terminal pairs $3 < I_Z < 10$	8.4±2.9	6.1±4.3	58.2±22.1	48.6±24.1	43.9±7.8
	Average I_Z	7.5±0.1	7.1±0.4	5.4±1.4	5.4±1.6	5.8±1.1
	Average g_s (nS) ($I_Z \rightarrow 10$)	11.5±2.9	14.9±1.9	12.2±4.8	8.7±3.8	8.6±2.1
	RMSE $_Z$ (M Ω)	6.6±1.1	8.5±0.9	11.1±4.5	9.7±2.3	16.1±5.1

Figure S3. Analysis of five classes of cortical cells (related to Fig 4). Five M-types from the BBP column were selected and analysed in detail. Three groups of properties were computed: morphometric, electrical and NET-related properties. As morphometric properties we selected the number of terminal branches, the number of main branches emanating from the soma and the total dendritic length. As electrical properties we selected the somatic input impedance Z_{soma} , the maximal input impedance Z_{in} along the dendritic arborization and the minimal transfer impedance Z_{trans} between any pair of locations. Regarding the NET-related properties, we calculated the average number of compartments at different values of $I_Z (= 1, 3, 10, 30)$. We also computed the percentage of terminal pairs that are separated by an I_Z between 3 and 10, the average I_Z of these pairs and the shunting conductance required to increase the I_Z of these pairs to 10. To check whether the NET approximation yielded accurate results, we also computed the root mean square error RMSE $_Z$ of the approximated impedance matrix with respect to the exact matrix. As can be seen, the error values we found are within similar ranges as those found for our three prototype cells (see Fig 1I). For each quantity, its average value and standard deviation is shown.

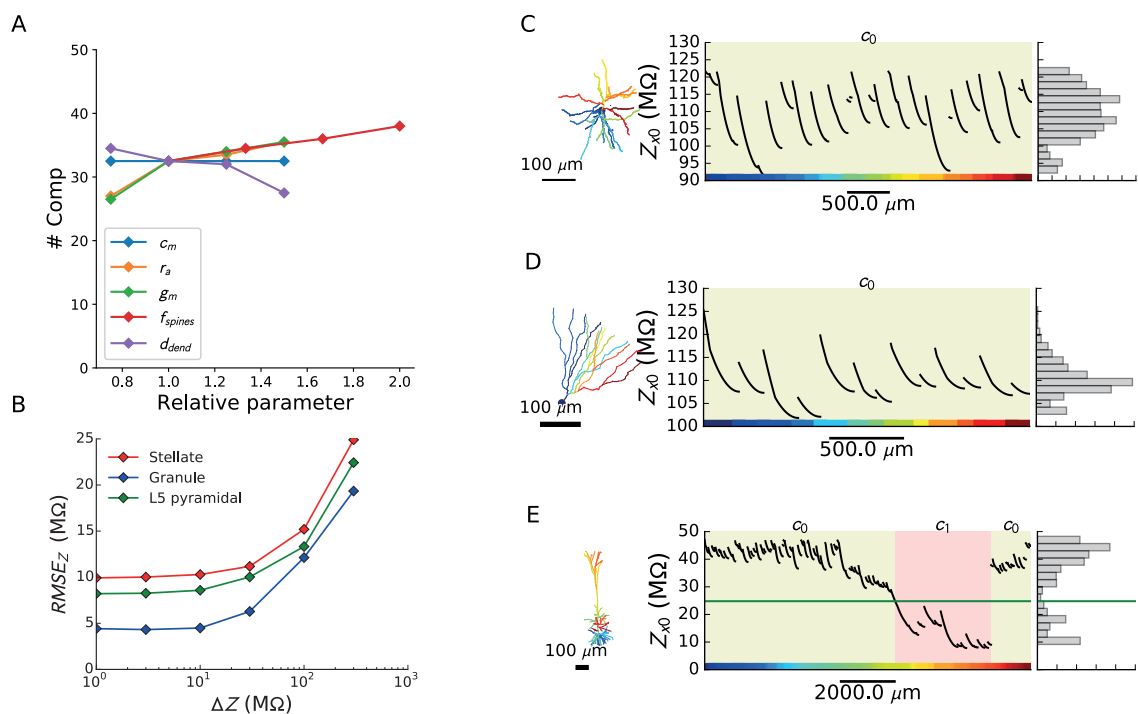


Figure S4. Extra information on compartment numbers and the derivation of a NET (related to methods). **A:** Analysis of the dependence of compartment numbers on a range of parameters for the L5.TTPC1 class of Fig S3. The x-axis represents the relative parameter value (compared to our standard set of parameters, see methods). c_m is membrane capacitance, r_a axial resistance, g_m membrane conductance, f_{spines} a spine correction factor (multiplied simultaneously to g_m and c_m in dendritic segments with radii below $0.6 \mu\text{m}$ to model the membrane surface increase due to spines) d_{dend} the diameter of the dendritic segments. **B:** The RMSE of the NET impedance matrix approximation compared to the true impedance matrix, as a function of ΔZ . **C-E:** For each row (C: stellate cell, D: granule cell and E: pyramidal cell), the morphology is shown on the left, the bottom row of the impedance matrix (i.e. the somatic transfer impedance Z_{0x}) in the middle, and a histogram of these impedance values on the right. The x-axis of the middle panel is coloured according to the corresponding region on the morphology. The background colouring indicates the different dendritic domains that will become nodes c_i in the NET, as found from the histograms on the right.

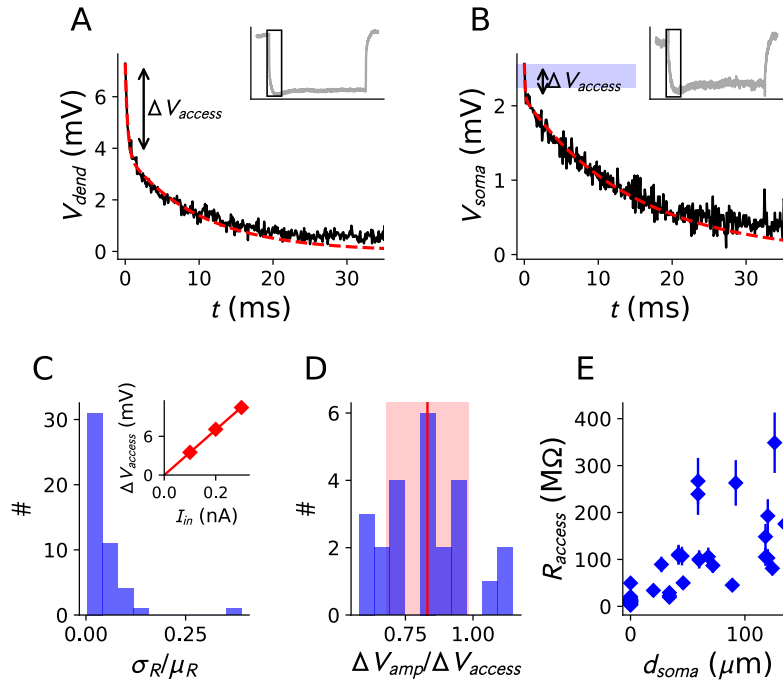


Figure S5. Estimation of the access resistance at the dendritic electrode (related to Fig 5). **A-B:** A double exponential (red dashed line) was fit to the transient part of the voltage response at the current injection electrode (black line, A resp. B for dendritic resp. somatic injection). The resulting fit was a combination of a fast and a slow exponential. The amplitude of the fast exponential was taken to be the voltage drop caused by the access resistance. At the somatic injection site (panel B) this amplitude was compared to the correction applied by the amplifier (height of blue square). **C:** Validation of the access resistance fit: for each recording, we extracted the voltage drop independently for all injected current amplitudes. We then compared the standard deviation of the access resistances obtained from each individual measurement (σ_R , obtained by dividing each point in the inset plot by the corresponding injected current) with the access resistance obtained from the slope of the best fit line (μ_R). We then plotted a histogram of the ratio of these values (where small numbers indicate co-linearity). **D:** Histogram of the ratios between the access resistance correction values applied by the amplifier and the values extracted from the double exponential fit at the somatic injection site. Mean (red line) and standard deviation (red rectangle) of this distribution were used to correct the access resistance values at the dendritic site obtained from the double exponential fit, and yielded the errorbars in voltage and input impedance (Fig 5C). **E:** Obtained access resistance values as a function of distance to soma.

Methods S1 (related to STAR methods)

Description of NET matrix inversion algorithm

On the one hand, the NET allows efficient simulation of the neuronal dynamics, and on the other hand it can be used to compute attractor points of these dynamics. The latter yield insight into the asymptotic behaviour of the neuron as a dynamical system and can be used to extract information about compartmentalization: for an instantaneous set of synaptic conductances $g_1(t), \dots, g_n(t)$, the instantaneous solution of the attractor point will be what the full dynamical system is trying to reach. Hence, if components of the attractor point solution behave independently from other components, the full dynamics will behave independently too. Both the full simulation and attractor point solution involve solving linear systems by matrix inversion. The NET tree graph structure allows this to be done in $O(n)$ steps, as opposed to $O(n^3)$ steps for arbitrary linear systems. We will first describe how the non-zero elements in this matrix are constructed for each solution method. Then we will describe the solution algorithm.

We will order the node voltages in the NET tree in a reversed depth-first manner (so that the root voltage comes last) and group them in a vector $\bar{\mathbf{V}}$. Similarly, the node impedances will be grouped in a vector $\bar{\mathbf{Z}}$. With each node N we will associate the set \mathcal{R}_N containing all input regions that a node integrates. Furthermore, with each input region r we will associate the set \mathcal{S}_r of all synapse types present in the input region and the set \mathcal{N}_r of all nodes that integrate inputs from that region. Although not strictly necessary, we assume for simplicity that each leaf only integrates inputs from one region and that each input region is first integrated by a leaf. With these assumptions, the sets \mathcal{N}_r always constitute paths from leaf to root, as is illustrated in Fig M1A. The general form of the synaptic input current at node N is then given by:

$$\bar{I}_N(t, \bar{\mathbf{V}}(t)) = \sum_{r \in \mathcal{R}_N} \sum_{s \in \mathcal{S}_r} g_s(t) f_s \left(\sum_{M \in \mathcal{N}_r} \bar{V}_M(t) \right). \quad (1)$$

We thus sum over all regions integrated by node N and all synapse types in these input regions, and the voltage in the SAD is given by the sum over all node voltages that integrate these input regions. Note that besides $\bar{\mathbf{V}}(t)$, the only other temporal dependence in $\bar{\mathbf{I}}(t, \bar{\mathbf{V}}(t))$ is through the synaptic conductances ($g_s(t)$, grouped in a vector \mathbf{g}). When convenient, we will therefore sometimes write $\bar{\mathbf{I}}_{\mathbf{g}(t)}(\bar{\mathbf{V}}(t))$. Finally, we remark that the set \mathcal{N}_r always denotes a direct path from leaf to root.

The full dynamical system.

The full dynamical system associated with the NET can be written in vector form as:

$$\bar{\mathbf{V}}(t) = \int_{-\infty}^t ds \bar{\mathbf{Z}}(t-s) \odot \bar{\mathbf{I}}(s, \bar{\mathbf{V}}(s)). \quad (2)$$

where \odot denotes element-wise multiplication. To solve a system of this form for $\bar{\mathbf{V}}(t+h)$ when $\bar{\mathbf{I}}(t-kh, \bar{\mathbf{V}}(t-kh))$ is known for $k = 0, 1, 2, \dots$, one can assume a linear interpolation between the grid points. Since the impedances $\bar{\mathbf{Z}}_N(t)$ are known as sums of exponentials, they can be integrated analytically in combination with the linear interpolation to obtain an accurate quadrature rule (section 2.2 in Wybo et al. (2015)). Grouping all terms that do not contain $\bar{\mathbf{V}}(t+h)$ in a term $\bar{\mathbf{F}}(t)$, one obtains:

$$\bar{\mathbf{V}}(t+h) = \bar{\mathbf{Z}}^{(0)} \odot \bar{\mathbf{I}}(t+h, \bar{\mathbf{V}}(t+h)) + \bar{\mathbf{F}}(t), \quad (3)$$

where $\bar{\mathbf{Z}}^{(0)}$ is a vector based on the impedance kernels that follows from the quadrature rule. Taylor expanding \bar{I}_N around $\bar{\mathbf{V}}(t)$ gives:

$$\bar{I}_N(t+h, \bar{\mathbf{V}}(t+h)) \approx \bar{\mathbf{I}}(t+h, \bar{\mathbf{V}}(t)) + \sum_M \left. \frac{\partial \bar{I}_N}{\partial \bar{V}_M} \right|_{t+h, \bar{\mathbf{V}}(t)} \left[\bar{V}_M(t+h) - \bar{V}_M(t) \right]. \quad (4)$$

Moving all terms containing components of $\bar{\mathbf{V}}(t+h)$ to the left hand side then gives a system of the form

$$\mathbb{A}(t+h)\bar{\mathbf{V}}(t+h) = \bar{\mathbf{B}}(t+h), \quad (5)$$

which can be solved for the node voltage. In this system, the vector $\bar{\mathbf{B}}(t+h)$ contains:

$$\bar{\mathbf{B}}_N(t+h) = \bar{\mathbf{Z}}_N^{(0)} \left[\bar{I}_N(t+h, \bar{\mathbf{V}}(t)) - \sum_M \frac{\partial \bar{I}_N}{\partial \bar{V}_M} \Big|_{t+h, \bar{\mathbf{V}}(t)} \bar{V}_M(t) \right] + \bar{\mathbf{F}}_N(t) \quad (6)$$

and the elements of matrix $\mathbb{A}(t+h)$ are given by:

$$A_{NM}(t+h) = \delta_{NM} - \bar{\mathbf{Z}}_N^{(0)} \frac{\partial \bar{I}_N}{\partial \bar{V}_M} \Big|_{t+h, \bar{\mathbf{V}}(t)}, \quad (7)$$

with δ_{NM} the Kronecker delta.

The attractor points.

The attractor points associated with (2) follow from the equality:

$$\bar{\mathbf{V}} = \bar{\mathbf{Z}} \odot \bar{\mathbf{I}}_g(\bar{\mathbf{V}}) \quad (8)$$

or equivalently:

$$\bar{\mathbf{H}}(\bar{\mathbf{V}}) := \bar{\mathbf{V}} - \bar{\mathbf{Z}} \odot \bar{\mathbf{I}}_g(\bar{\mathbf{V}}) = 0 \quad (9)$$

and can be found from the Newton iteration (with k the iteration index):

$$\mathbb{A}_{\bar{\mathbf{H}}(\bar{\mathbf{V}}_k)} \bar{\mathbf{V}}_{k+1} = \bar{\mathbf{B}}_k, \quad (10)$$

with $\mathbb{A}_{\bar{\mathbf{H}}(\cdot)}$ the Jacobian of $\bar{\mathbf{H}}(\cdot)$ and the right-hand side of this equation given by:

$$\bar{\mathbf{B}}_k = -\bar{\mathbf{H}}(\bar{\mathbf{V}}_k) + \mathbb{A}_{\bar{\mathbf{H}}(\bar{\mathbf{V}}_k)} \bar{\mathbf{V}}_k. \quad (11)$$

The elements of the Jacobian are:

$$A_{NM} = \delta_{NM} - \bar{\mathbf{Z}}_N \frac{\partial \bar{I}_{g,N}}{\partial \bar{V}_M}(\bar{\mathbf{V}}_k). \quad (12)$$

The matrix inversion.

From (7) and (12) it can be seen that systems (5) and (10) have the same structure, the only difference being that in (7) constants $\bar{\mathbf{Z}}_N^{(0)}$ are employed that follow from the quadrature rule whereas in (12) the node impedances $\bar{\mathbf{Z}}_N$ are used. The NET tree now imposes a very special structure on the matrix \mathbb{A} that allows it to be inverted in $O(n)$ steps. First, the algorithm performs a single down sweep that sets all elements under the diagonal to zero. Then, a single up sweep is performed to set all elements above the diagonal to zero. To construct \mathbb{A} , we start from the identity matrix and then subtract

$$\bar{\mathbf{Z}}_N \frac{\partial \bar{I}_{g,N}}{\partial \bar{V}_M} = \bar{\mathbf{Z}}_N \sum_{r \in \mathcal{N}_N} \left[\sum_{s \in \mathcal{N}_r} \left(g_s f'_s \left(\sum_{K \in \mathcal{N}_r} \bar{V}_K \right) \right) \sum_{K \in \mathcal{N}_r} \delta_{KM} \right] \quad (13)$$

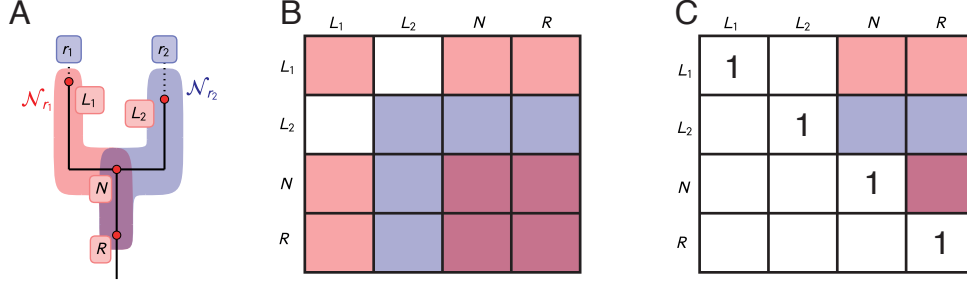


Figure M1. Schematic representation of the inversion algorithm. A: A schematic of a simple NET with four nodes L_1, L_2, N and R , two input regions r_1 and r_2 , and the two paths \mathcal{N}_{r_1} and \mathcal{N}_{r_2} coloured red and blue respectively (mixed colour purple indicates that the two paths overlap). **B:** The structure of the associated matrix \mathbb{A} as obtained from equation (13). **C:** By a recursive series of row operations the sub-diagonal elements of \mathbb{A} are set to zero, while the diagonal elements are at the same time set to one. After the down sweep, the root voltage can be computed directly. Other voltages are then computed during the up sweep.

for all N, M . Here, f'_s denotes the derivative of f_s . Dissecting this, we see that for each path \mathcal{N}_r , the rows corresponding to the nodes $N \in \mathcal{N}_r$ contain a term $-\bar{Z}_N \left[\sum_{s \in \mathcal{N}_r} g_s f'_s \left(\sum_{K \in \mathcal{N}_r} \bar{V}_K \right) \right]$ at each column associated with a node in \mathcal{N}_r . This leads to a structure that is depicted in Fig M1B. To simplify the notation, we will denote the term in square brackets by:

$$a(\mathcal{N}_r) := \sum_{s \in \mathcal{N}_r} g_s f'_s \left(\sum_{K \in \mathcal{N}_r} \bar{V}_K \right). \quad (14)$$

We will also group all terms in columns associated with \mathcal{N}_r in row N of the matrix in a vector $\mathbf{R}(N)|_{\mathcal{N}_r}$, that thus contains

$$\left(\mathbf{R}(N)|_{\mathcal{N}_r} \right)_K = \delta_{NK} - \bar{Z}_N a(\mathcal{N}_r), \quad \text{for } K \in \mathcal{N}_r. \quad (15)$$

For instance, in Fig M1B, $\mathbf{R}(L_1)|_{\mathcal{N}_{r_1}}$ is given by the red elements on the first line of the matrix, and similarly for nodes N and R . In turn, rows $\mathbf{R}(\cdot)|_{\mathcal{N}_{r_2}}$ associated with \mathcal{N}_{r_2} are coloured blue for nodes L_2, N and R .

Finally, we introduce for formal reasons a term $b(\mathcal{N}_r)$ that is zero in the first step of the algorithm, so that the elements of the vector \mathbf{B} become:

$$\left(\bar{\mathbf{B}} \right)_N = \bar{B}_N - \bar{Z}_N \sum_{r \in \mathcal{N}_N} b(\mathcal{N}_r), \quad (16)$$

and similarly to $\mathbf{R}(N)|_{\mathcal{N}_r}$, we will take $\left(\bar{\mathbf{B}}|_{\mathcal{N}_r} \right)$ to signify the restriction of $\bar{\mathbf{B}}$ to terms only in \mathcal{N}_r :

$$\left(\bar{\mathbf{B}}|_{\mathcal{N}_r} \right)_N = \bar{B}_N - \bar{Z}_N b(\mathcal{N}_r). \quad (17)$$

First, we describe the steps of the down sweep phase of the algorithm.

1. We take the leaf L of a path \mathcal{N}_r , divide row L by its diagonal element and obtain:

$$\left(\mathbf{R}(L)|_{\mathcal{N}_r} \right)_K = \begin{cases} \frac{-\bar{Z}_L a(\mathcal{N}_r)}{1 - \bar{Z}_L a(\mathcal{N}_r)} & \text{if } K \neq L \\ 1 & \text{if } K = L, \end{cases} \quad (18)$$

Correspondingly,

$$\left(\bar{\mathbf{B}}\right)_L = \frac{\bar{B}_L - \bar{Z}_L b(\mathcal{N}_r)}{1 - \bar{Z}_L a(\mathcal{N}_r)}. \quad (19)$$

On all rows $N \in \mathcal{N}_r \setminus \{L\}$ we effectuate the row operation

$$\begin{aligned} \mathbf{R}(N) &\rightarrow \mathbf{R}(N) - \left(\mathbf{R}(N)|_{\mathcal{N}_r}\right)_L \mathbf{R}(L) \\ \left(\bar{\mathbf{B}}\right)_N &\rightarrow \left(\bar{\mathbf{B}}\right)_N - \left(\mathbf{R}(N)|_{\mathcal{N}_r}\right)_L \left(\bar{\mathbf{B}}\right)_L. \end{aligned} \quad (20)$$

This operation sets sub-diagonal elements $\left(\mathbf{R}(N)|_{\mathcal{N}_r}\right)_L$ to zero. For the non-zero elements $M \neq L$ we obtain:

$$\begin{aligned} \left(\mathbf{R}(N)|_{\mathcal{N}_r}\right)_M &= \delta_{NM} - \bar{Z}_N a(\mathcal{N}_r) - \left(-\bar{Z}_N a(\mathcal{N}_r)\right) \frac{-\bar{Z}_L a(\mathcal{N}_r)}{1 - \bar{Z}_L a(\mathcal{N}_r)} \\ &= \delta_{NM} - \bar{Z}_N \frac{a(\mathcal{N}_r)}{1 - \bar{Z}_L a(\mathcal{N}_r)}, \end{aligned} \quad (21)$$

while

$$\begin{aligned} \left(\bar{\mathbf{B}}|_{\mathcal{N}_r}\right)_N &= \bar{B}_N - \bar{Z}_N b(\mathcal{N}_r) - \left(-\bar{Z}_N a(\mathcal{N}_r)\right) \frac{\bar{B}_L - \bar{Z}_L b(\mathcal{N}_r)}{1 - \bar{Z}_L a(\mathcal{N}_r)} \\ &= \bar{B}_N - \bar{Z}_N \frac{b(\mathcal{N}_r) - \bar{B}_L a(\mathcal{N}_r)}{1 - \bar{Z}_L a(\mathcal{N}_r)}. \end{aligned} \quad (22)$$

Let P be the parent node of L in the path \mathcal{N}_r . If all sub-diagonal elements for paths associated with regions in \mathcal{R}_P have been set to zero, one can move on to step 2 with node P . Otherwise repeat step 1 with a different leaf and path until such is the case.

2. Consider all $r \in \mathcal{R}_P$. We will denote the restriction of the path \mathcal{N}_r to nodes from P to the root as $\mathcal{N}_r^{P\downarrow}$. The tree structure imposes that all these paths are the same:

$$\mathcal{N}_{r_1}^{P\downarrow} = \mathcal{N}_{r_2}^{P\downarrow}, \quad \forall r_1, r_2 \in \mathcal{R}_P. \quad (23)$$

Hence we will use the shorthand:

$$\mathcal{N}_P := \mathcal{N}_r^{P\downarrow}. \quad (24)$$

As a consequence of step 1, it holds for all $N \in \mathcal{N}_P$ that:

$$\left(\mathbf{R}(N)|_{\mathcal{N}_P}\right)_M = \delta_{NM} - \bar{Z}_N \sum_{r \in \mathcal{R}_P} \frac{a(\mathcal{N}_r)}{1 - \bar{Z}_{L_r} a(\mathcal{N}_r)}, \quad (25)$$

where L_r signifies the leaf associated with the path \mathcal{N}_r , and that:

$$\left(\bar{\mathbf{B}}|_{\mathcal{N}_P}\right)_N = \bar{B}_N - \bar{Z}_N \sum_{r \in \mathcal{R}_P} \frac{b(\mathcal{N}_r) - \bar{B}_{L_r} a(\mathcal{N}_r)}{1 - \bar{Z}_{L_r} a(\mathcal{N}_r)}. \quad (26)$$

We can now define

$$a(\mathcal{N}_P) := \sum_{r \in \mathcal{R}_P} \frac{a(\mathcal{N}_r)}{1 - \bar{Z}_{L_r} a(\mathcal{N}_r)} \quad (27)$$

and

$$b(\mathcal{N}_P) := \sum_{r \in \mathcal{R}_P} \frac{b(\mathcal{N}_r) - \bar{B}_{L_r} a(\mathcal{N}_r)}{1 - \bar{Z}_{L_r} a(\mathcal{N}_r)}. \quad (28)$$

With these substitutions, we are now able to formally proceed with the algorithm as if P was a leaf and \mathcal{N}_P the path to it. We may thus return to step 1, unless P was the root of the tree, in which case its associated voltage is known:

$$\bar{V}_P = \frac{\bar{B}_P - \bar{Z}_P b(\mathcal{N}_P)}{1 - \bar{Z}_P a(\mathcal{N}_P)}. \quad (29)$$

The structure of the matrix after the down sweep is illustrated in Fig M1C.

Note that the efficiency of the algorithm lies in the fact that we do not have to do the row operation (20) explicitly for each node N on the path to the root. It suffices to compute the quantities $a(\mathcal{N}_P)$ and $b(\mathcal{N}_P)$ once for each node that is not a leaf.

For the up sweep of the algorithm, we assume that we have a node P for which the voltages associated with nodes in \mathcal{N}_P (i.e. the path from P down to the root) are known. Then performing, for all nodes N in the sub-tree of P , the row operation:

$$\begin{aligned} \mathbf{R}(N) &\rightarrow \mathbf{R}(N) - (\mathbf{R}(N))_P \mathbf{R}(P) \\ (\bar{\mathbf{B}})_N &\rightarrow (\bar{\mathbf{B}})_N - (\mathbf{R}(N))_P (\bar{\mathbf{B}})_P \end{aligned} \quad (30)$$

sets the supra-diagonal elements $(\mathbf{R}(N)|_{\mathcal{N}_P})_P$ to zero. Repeating this operation with the child nodes C of P sets their associated supra-diagonal elements $(\mathbf{R}(N)|_{\mathcal{N}_C})_C$ to zero, with N now in the sub-tree of C . Continuing so until the leaves are reached diagonalizes the whole matrix.

Key here is that we do not have to do all the row operations explicitly either; from equation (25) it follows that all supra-diagonal elements on a given row are the same. Hence, the voltage associated with a node N with parent P is given by:

$$\bar{V}_N = \frac{\bar{B}_N - \bar{Z}_N b(\mathcal{N}_N)}{1 - \bar{Z}_N a(\mathcal{N}_N)} + \frac{\bar{Z}_N a(\mathcal{N}_N)}{1 - \bar{Z}_N a(\mathcal{N}_N)} \left(\sum_{K \in \mathcal{N}_P} \bar{V}_K \right) \quad (31)$$

and recursion can proceed with the child nodes of N .

To conclude, we summarize the algorithm in the pseudo code in Fig M2.

Matrix inversion with linear terms.

To extend the matrix inversion algorithm to the system with linear terms (LinT), we note that the rows in the Jacobian associated with nodes that integrate the AP current receive extra terms. For each region r , and for all nodes K on the path \mathcal{N}_r , the following terms are added to rows associated with all nodes N integrating the AP current:

$$\left(\mathbf{R}(N)|_{\mathcal{N}_r} \right)_K^{\text{LinT}} = -\bar{Z}_N I'_{AP} \sum_r \bar{Z}_r a(\mathcal{N}_r), \quad (32)$$

For ease of notation we will define a quantity α_r :

$$\alpha_r = \sum_r \bar{Z}_r a(\mathcal{N}_r), \quad (33)$$

as well as a term β_r that is zero in the first step of the down sweep algorithm,

$$\left(\bar{\mathbf{B}}|_{\mathcal{N}_r} \right)_N^{\text{LinT}} = -\bar{Z}_N I'_{AP} \beta_r. \quad (34)$$

The steps of the down sweep phase of the extended inversion algorithm proceed in the same way as in the normal inversion algorithm, but with the following additional operations:

```

Procedure Down sweep (leaf L)
1  if L is true leaf then
2      compute  $a(\mathcal{N}_l)$ 
3       $b(\mathcal{N}_l) \leftarrow 0$ 
4  end
5  compute  $B_L$  according to integration
   paradigm
6  store  $B_L, \bar{a}(\mathcal{N}_l), b(\mathcal{N}_l)$  at node L
7  if L not root then
8      retrieve parent P
9       $a(\mathcal{N}_P) += \frac{a(\mathcal{N}_l)}{1 - \bar{Z}_l a(\mathcal{N}_l)}$ 
10      $b(\mathcal{N}_P) += \frac{b(\mathcal{N}_l) - \bar{B}_l a(\mathcal{N}_l)}{1 - \bar{Z}_l a(\mathcal{N}_l)}$ 
11 end
12 if all children of P have been passed
   then
13     if P is not root then
14          $L \leftarrow P$ 
15         Down sweep (L)
16     end
17 else
18     Stop recursion
19 end
20 end

```

Input: leaf *L*

Down sweep (*L*)

```

Procedure Up sweep (node N, voltage
VP)
1   $\bar{V}_N \leftarrow \frac{\bar{B}_N - \bar{Z}_N b(\mathcal{N}_n)}{1 - \bar{Z}_N a(\mathcal{N}_n)} + \frac{\bar{Z}_N a(\mathcal{N}_n)}{1 - \bar{Z}_N a(\mathcal{N}_n)} V_P$ 
2   $a(\mathcal{N}_n) \leftarrow 0, b(\mathcal{N}_n) \leftarrow 0, B_N \leftarrow 0$ 
3  for childnodes C of N do
4      Up sweep (C, VP +  $\bar{V}_N$ )
5  end

```

Input: root *R*

Up sweep (*R, 0*)

Figure M2. Pseudocode for the up and down sweep phases of the matrix inversion algorithm. During both phases, each node is passed exactly once.

1. After dividing the row associated with the leaf l of the path \mathcal{N}_r by its diagonal element, as in (18), we effectuate the following row operation on all rows associated with nodes N that integrate the somatic input:

$$\begin{aligned} \mathbf{R}(N) &\rightarrow \mathbf{R}(N) - \left(\mathbf{R}(N)|_{\mathcal{N}_r}\right)_L^{\text{LinT}} \mathbf{R}(L) \\ \left(\bar{\mathbf{B}}\right)_N &\rightarrow \left(\bar{\mathbf{B}}\right)_N - \left(\mathbf{R}(N)|_{\mathcal{N}_r}\right)_L^{\text{LinT}} \left(\bar{\mathbf{B}}\right)_L \end{aligned} \quad (35)$$

which sets the term $\left(\mathbf{R}(N)|_{\mathcal{N}_r}\right)_L^{\text{LinT}}$ to zero. The remaining non-zero terms in row N are then:

$$\left(\mathbf{R}(N)|_{\mathcal{N}_r}\right)_K^{\text{LinT}} = -\bar{Z}_N l'_{AP} \alpha_r \left(1 - \frac{a(\mathcal{N}_r)}{1 - \bar{Z}_L a(\mathcal{N}_r)}\right) \quad (36)$$

and

$$\left(\bar{\mathbf{B}}|_{\mathcal{N}_r}\right)_N^{\text{LinT}} = -\bar{Z}_N l'_{AP} \left(\beta_r - \frac{\alpha_r \bar{B}_L}{1 - \bar{Z}_L a(\mathcal{N}_r)}\right). \quad (37)$$

2. In step 2, we then define the following additional quantities associated with node P :

$$\alpha_p := \sum_{r \in \mathcal{R}_P} \alpha_r \left(1 - \frac{a(\mathcal{N}_r)}{1 - \bar{Z}_L a(\mathcal{N}_r)}\right) \quad (38)$$

and

$$\beta_p := \sum_{r \in \mathcal{R}_P} \left(\beta_r - \frac{\alpha_r \bar{B}_L}{1 - \bar{Z}_L a(\mathcal{N}_r)}\right). \quad (39)$$

The up sweep phase of the algorithm then proceeds in the same way as before for the nodes that do not integrate the somatic region.

Analytical results with conductance-based synapses

The terms in $\bar{\mathbf{I}}_g(\bar{\mathbf{V}})$ corresponding to AMPA and GABA synapses depend linearly on the voltage through the driving force. When only such synapses are present, the Newton iteration (10) yields the true node voltages in a single step, while at the same time providing insight in the input/output relation of the neuron. We describe this input/output relation in the next paragraph for the case where only a single synapse type is present, although the extension to multiple synapse types is possible. Furthermore, we show that in certain cases, a shunting input can be seen as reducing the impedance associated with specific nodes in the NET tree. We also discuss the relation with the shunt level, a quantity used previously to quantify shunting interactions in dendritic trees (Gidon and Segev, 2012).

A simple input/output transformation.

When a single synapse type with linear voltage dependence is present on the dendritic tree, equation (1) becomes:

$$\bar{I}_{N,g}(\bar{\mathbf{V}}) = \sum_{r \in \mathcal{R}_N} g_r \left(E_r - V_{\text{eq}} - \sum_{K \in \mathcal{N}_r} \bar{V}_K \right), \quad (40)$$

where E_r denotes the synaptic reversal potential and V_{eq} the equilibrium voltage. For the sake of brevity, we will group these time-independent potentials in a single variable :

$$E := E_r - V_{\text{eq}} \quad (41)$$

The elements of matrix \mathbb{A} in (10) have the form:

$$A_{NM} = \delta_{NM} + \bar{Z}_N \sum_{r \in \mathcal{R}_N} g_r \sum_{K \in \mathcal{N}_r} \delta_{KM} \quad (42)$$

whereas for the contents of vector $\bar{\mathbf{B}}$ (with $\bar{V}_0 = 0$) we find:

$$\bar{B}_N = Z_N \sum_{r \in \mathcal{R}_N} g_r E. \quad (43)$$

For the rows of \mathbb{A} , this means that:

$$\left(\mathbf{R}(N) |_{\mathcal{N}_r} \right)_K = \delta_{NK} + \bar{Z}_N g_r, \quad \text{for } K \in \mathcal{N}_r. \quad (44)$$

In step 2 of the down sweep algorithm, with these simplifications it holds that:

$$\left(\mathbf{R}(N) |_{\mathcal{N}_p} \right)_M = \delta_{NM} + Z_N \sum_{r \in \mathcal{R}_p} \frac{g_r}{1 + Z_{L_r} g_r} \quad (45)$$

and

$$\begin{aligned} \left(\bar{\mathbf{B}} |_{\mathcal{N}_r} \right)_N &= \bar{B}_N - \sum_{r \in \mathcal{V}_p} \bar{Z}_N g_r \frac{Z_{L_r} g_r E}{1 + Z_{L_r} g_r} \\ &= \bar{Z}_N \sum_{r \in \mathcal{R}_p} g_r E - \sum_{r \in \mathcal{R}_p} \bar{Z}_N g_r \frac{Z_{L_r} g_r E}{1 + Z_{L_r} g_r} \\ &= \bar{Z}_N \sum_{r \in \mathcal{R}_p} \frac{g_r}{1 + Z_{L_r} g_r} E. \end{aligned} \quad (46)$$

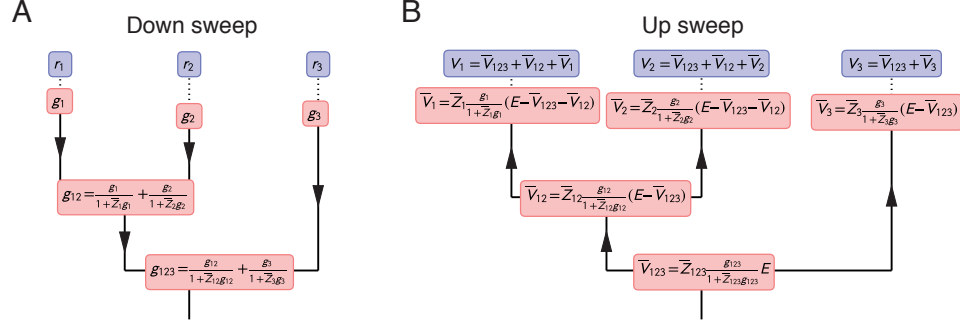


Figure M3. Solution for a single synapse type. A: In the down sweep phase, the conductances are rescaled by a shunt factor. **B:** The up sweep sets all the node voltages.

This suggest that instead of equation (27), we can now define:

$$g_p := \sum_{r \in \mathcal{R}_p} \frac{g_r}{1 + \bar{Z}_r g_r}, \quad (47)$$

and, since this factor occurs both in (45) and (46), we may consider it as a synaptic conductance associated with node P . With respect to the downward recursion, P then formally becomes a leaf of the tree. If P is the root of the tree, its voltage is given by:

$$\bar{V}_P = \bar{Z}_P \frac{g_P}{1 + \bar{Z}_P g_P} E. \quad (48)$$

The up sweep then proceeds as in the full algorithm, but instead of equation (31), we find:

$$\bar{V}_N = \bar{Z}_N \frac{g_N}{1 + \bar{Z}_N g_N} \left(E - \sum_{K \in \mathcal{N}_P} \bar{V}_K \right). \quad (49)$$

This solution is depicted in Fig M3 for a simple NET tree. It can be seen that the conductance associated with the root node is given by a combination of shunting non-linearities

$$F_Z(g) = \frac{g}{1 + Zg} \quad (50)$$

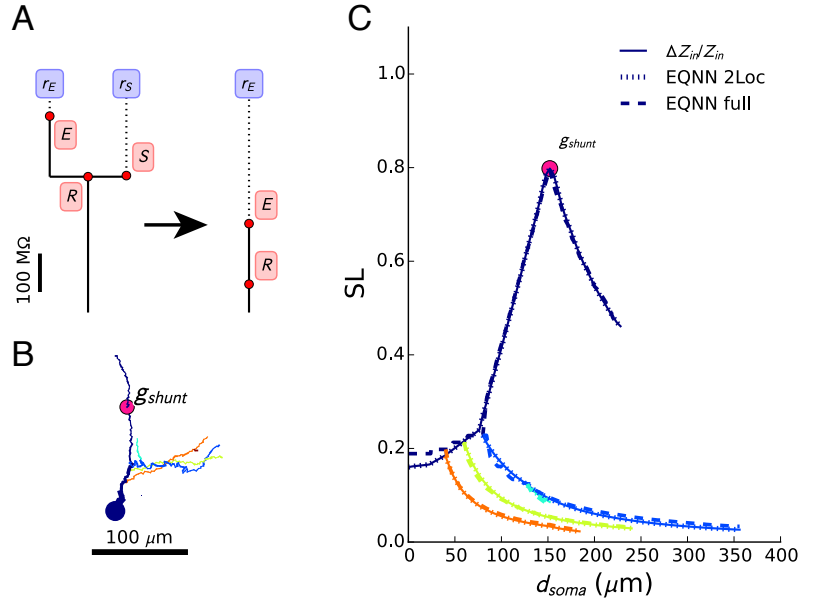
and linear sums (Fig M3A), and that the root voltage can be computed directly from knowledge of the associated conductance. This parallels the way the output is constructed in artificial neural networks (ANN's). The amount of shunting in a node is furthermore proportional to the impedance in that node. If conductance and/or impedance are small, so that $Zg \ll 1$ in all nodes, the root voltage is simply a linear sum of all the inputs. If local voltages need to be known, the up sweep is straightforward to compute, as depicted in Fig M3B.

Shunting.

Shunting inhibition has proven to be a powerful tool to modulate the output of regions in the dendritic arborization (Gidon and Segev, 2012). The influence of this shunt on other dendritic regions can be quantified by the shunt level SL , i.e. the relative reduction in input impedance:

$$SL = \frac{\Delta Z_{in}}{Z_{in}}. \quad (51)$$

Figure M4. SL in a subtree of a stellate cell. **A:** Schematic NET with a region of excitation r_E and a region of shunting r_S . The shunt can be eliminated from the NET by rescaling the conductance of the root R . **B:** The dendritic subtree. **C:** SL computed according to the normal definition (labelled $\Delta Z_{in}/Z_{in}$), the exact two location NET (labelled 2Loc) and an approximate NET pruned from the full NET tree (labelled full). Colours correspond to the colour code in B.



It is instructive to understand the analytical NET formula for this shunt level. The original NET system has the following form:

$$\begin{aligned}\bar{V}_E &= \bar{Z}_E g_E \cdot f(\bar{V}_R + \bar{V}_E) \\ \bar{V}_S &= -\bar{Z}_S g_S \cdot (\bar{V}_R + \bar{V}_S) \\ \bar{V}_R &= \bar{Z}_R \left[g_E \cdot f(\bar{V}_R + \bar{V}_E) - g_S \cdot (\bar{V}_R + \bar{V}_S) \right],\end{aligned}\tag{52}$$

where the subscript E denotes a node associated with only excitation, S a node with only shunting inhibition and R the root node that combines both synapses. Solving for shunt-related terms gives:

$$\begin{aligned}\bar{V}_E &= \bar{Z}_E g_E \cdot f(\bar{V}_R + \bar{V}_E) \\ \bar{V}_S &= -\frac{\bar{Z}_S}{1 + \bar{Z}_S g_S} g_S \bar{V}_R \\ \bar{V}_R &= \frac{\bar{Z}_R}{1 + \bar{Z}_R \frac{g_S}{1 + \bar{Z}_S g_S}} \left[g_E \cdot f(\bar{V}_R + \bar{V}_E) \right].\end{aligned}\tag{53}$$

Formally, the first and last equations in this system can now be seen as an NET with a single input region and a root impedance that is modified due to the shunt conductance g_S , as is illustrated in Fig M4A. From the original input impedance at the excitatory synapse $\bar{Z}_E + \bar{Z}_R$ and the new input impedance $\bar{Z}_E + \frac{\bar{Z}_R g_S}{1 + \bar{Z}_R \frac{g_S}{1 + \bar{Z}_S g_S}}$, the shunt level can be computed:

$$SL = \frac{\overbrace{\bar{Z}_R g_S}^1}{\underbrace{\left(1 + \frac{\bar{Z}_E}{\bar{Z}_R}\right)}_2 \underbrace{\left(1 + (\bar{Z}_R + \bar{Z}_S) g_S\right)}_3}.\tag{54}$$

It can be seen from factor 1 in the above formula that SL is proportional to the impedance in the common node as well as the shunt conductance. However, SL can not grow indeterminately, due to the saturation factor 3. The maximal shunt level is thus inversely proportional to the input impedance at the shunting synapse, $\bar{Z}_R + \bar{Z}_S$. Finally, due to factor 2, the amount of shunting also depends on the ratio between impedance at the excitatory node versus impedance at the root node. We computed SL for a subtree of a stellate cell (Fig M4B), once using the definition (51), and once using the NET derived for two locations. Since this NET is exact, these two lines coincide perfectly. We also computed SL once for an NET tree obtained from the recursive algorithm by pruning all unneeded regions. This approximate tree agrees very well with the true SL , thus serving as a further validation that our full NET tree can capture the interactions within a dendritic arborization accurately.